



## Flow topology of a container train wagon subjected to varying local loading configurations



Chao Li<sup>a,\*</sup>, David Burton<sup>a</sup>, Michael Kost<sup>b</sup>, John Sheridan<sup>a</sup>, Mark C. Thompson<sup>a</sup>

<sup>a</sup> Department of Mechanical and Aerospace Engineering, Monash University, Melbourne, Victoria, Australia

<sup>b</sup> Pacific National, Melbourne, Victoria, Australia

### ABSTRACT

How the positioning and length of a container placed on an arbitrary train wagon in an otherwise fully loaded train affects the local aerodynamics, and consequently the contribution to drag, is examined here. Results from scale-model wind-tunnel tests undertaken at a Reynolds number of  $0.3 \times 10^6$  for a combination of 49 upstream and downstream gap spacings ( $G_f, G_r$ ) are presented. Surface flow topology, pressure profiles and planar velocity fields are measured.  $G_r$  dominated the drag variations, with  $G_f$  only causing a secondary effect. The greatest drag reduction potential is found between gaps size of  $1.77W$  and  $3.23W$ , where  $W$  represents the wagon width. Over the range of  $G_f$  and  $G_r$  investigated, a number of distinct physical mechanisms were observed. These affect the separation size and the nature of boundary layer enveloping the wagon, which have a direct impact on the entrainment and shedding frequency of the wake.

### 1. Introduction

Significant opportunities exist to improve freight train fuel economy and operational safety through aerodynamic advancement. The bluntness of the locomotives and containers together with their extremely long bodies contribute to the aerodynamic drag they experience. Despite being considered a low-speed transport solution, over the large distances they travel in countries such as Australia, cruising velocities can reach 115 km/h, speeds at which aerodynamic drag can contribute more than 80% of total drag.

Intermodal freight trains are specialised trains used to carry intermodal containers (i.e., shipping containers). Such containers come in a wide range of sizes, commonly carried by *flat-cars*, *well-cars* and *skeletonised* cars of varying dimensions. This is in direct contrast to conventional passenger trains with cars (carriages) of repeating geometries. As each train is loaded differently, each train has a unique geometry and aerodynamic performance. Containers are often double-stacked, of particular interest to this study, which substantially changes the ratio of height-to-width. Furthermore, over the course of a cross-continental journey, the loading configuration of the train may change significantly as containers are loaded and unloaded at intermediate hubs. As a result, freight-train aerodynamic drag depends on loading configurations. Each train will have a different form that will vary from journey to journey, meaning it makes little sense to study a

specific loading configuration. Rather, if we can simplify the train geometry to be a summation of individual wagons, where the aerodynamic properties of each wagon is determined from its upstream and downstream flow condition, then we can better understand the overall train aerodynamics. If this were possible then this complex problem becomes amenable to simplification by characterising the aerodynamic profile of individual wagons under different loading configurations separately. Lai et al. (2008a, 2008b) have used such an incremental approach to develop a loading algorithm that takes account of aerodynamic factors. Further benefit can be gained from such algorithms with a more in-depth study of the details of the flow topology in the neighbourhood of the wagon, and further quantification of the drag penalties induced.

In addition to their complex geometry, intermodal freight trains can span lengths of 1.8 km with a length-to-height ratio in excess of  $L/H = 300$  (Gielow and Furlong, 1988; Lai and Barkan, 2005). This is significantly higher than that of other trains, such as high-speed trains, which typically are of the order of  $L/H = 100$  (Baker et al., 2014). The side and roof length over which the boundary layer develops cannot be reproduced with a short train model conventionally tested experimentally or numerically. An alternative approach, which we take here, is to view the aerodynamic drag of an individual wagon to be a combined effect of its local loading configuration and a surface boundary layer profile reflective of its longitudinal position within the train.

\* Corresponding author.

E-mail address: [chao.li@monash.edu](mailto:chao.li@monash.edu) (C. Li).

### 1.1. Wagon position within train

Gielow and Furlong (1988) have conducted direct measurements of the drag force experienced by an “AERO” car located from the second to the thirtieth wagon position within a train. They used a modified full-scale flat-car, serving as a support frame for a light-weight aluminium gondola body. A load cell was mounted between gondola body and the car frame, allowing direct force measurements of the gondola body. When the top gondola was covered, which is geometrically similar to a container wagon, it was shown that drag drops off exponentially as its position in the train moves downstream from the leading wagon. The drag contribution reached equilibrium from approximately the eighth position from the nose.

Wind tunnel testing by Watkins and Saunders suggested that to model a single wagon located within the middle section of a train only 1.5 wagons are required upstream and 0.5 wagons downstream. Any additional wagons added to the front and the rear has no significant impact on the drag value measured on the middle wagon. A numerical investigation by Golovanevskiy et al. (2012) showed that, excluding the three wagons located at the front and at the tail of the train, all other wagons within the middle region of the train displayed similar drag coefficients.

Soper et al. (2014) showed that slipstream growth stabilises quickly for a fully loaded train, but for a partially loaded train, slipstream continued to grow past the train length of 101.25 m. Full-scale slipstream measurements, taken as part of the RAPIDE project (Sterling et al., 2008), have displayed that the slipstream growth over a 700 m freight train is rapid and stabilises beyond 150 m.

Despite these studies, the nature of the boundary layer along an intermodal freight train, and how it varies for different loading configurations and prevailing wind, is not well understood. Nevertheless, the above work indicates that with sufficient upstream and downstream wagons an acceptable representation of an individual wagon's drag within a train can be obtained.

### 1.2. Wagon gap/spacing

Earlier research considered the effect of wagon-to-wagon gaps (spacing between wagons or containers) on an individual wagon and the overall train drag. The general consensus reached is that an increase in gap size and number of gaps within the train will increase the drag penalty.

Engdahl et al. (1987a, 1987b) conducted scaled wind-tunnel testing using a three-car arrangement, where the middle car was connected to a force balance. Properties such as inter-wagon gap, trailer front-end shape, and rail-car streamlining were explored. They concluded that while a drag increase is observed with larger inter-wagon gaps, the drag growth experienced is not linear, but neither were there any sudden shifts in the drag profile.

Watkins and Saunders (Watkins et al., 1992; Watkins and Saunders) investigated hopper and gondola rail wagons (loose-stock wagons), including the effect of inter-wagon gaps, crosswind angle, and the effect of various aerodynamic add-ons. Drag increases with respect to crosswind angle were found to be parabolic, and an increase in inter-wagon gap size consistently increased drag at each crosswind angle, thereby maintaining the same parabolic shape of the curve.

Östh and Krajnović (2014) used Large Eddy Simulations (LES) to model the flow over a single-stacked container wagon in free-stream, and with the wagon within a train. The second case was achieved using periodic boundary conditions. In a time-averaged sense, the flow regime of the wagon in free-stream consisted of vortices just behind the leading-edge corners on top and side surfaces. The wake has two vortices in the vertical plane, with the bottom vortex impinging on the rear surface. A symmetrical vortex pair was identified in the horizontal plane. The drag coefficient of the wagon when included in the train was found to be 90% lower than a wagon in free-stream. They explained the difference as a consequence of having two counter-rotating vortices in the gap, causing

the train to appear as one single body to the oncoming flow. However, no further wagon spacing was considered in that study.

### 1.3. Surface mounted cubes in tandem

The canonical studies of surface-mounted cubes (Castro and Robins, 1977; Castro, 1981) provide important reference data for sharp-edged three-dimensional objects, such as wagons. There have been extensive studies of the flow over surface-mounted cubes in tandem, analogous to multiple wagons aligned in succession (Havel et al., 2001; Martinuzzi and Havel, 2000, 2004; Sakamoto and Haniu, 1988). In general, three flow regimes exist for 3D cubes, depending on the gap spacing between the two cubes. Those regimes are denoted as the *bistable* regime, *lock-in* regime and *quasi-isolated* regime.

1. Bistable Regime: This regime occurs at a gap length of approximately  $1.5W$ , and results in two distinct frequency peaks appearing in the power spectrum of the surface pressure and wake velocity measurements. The driving mechanism is whether the shear layer separating from the leading edge of the first body reattaches to the sides of the downstream body. If no attachment occurs, a low frequency shedding occurs. However, if reattachment does occur, vortex shedding of higher frequency will be induced downstream of the second body. The downstream body experiences a gradual increase in drag, and the drag of the upstream body falls slowly to a minimum at a gap length of  $2W$ , after which it rises steadily.
2. Lock-in regime: This regime occurs for normalised gap length of  $1.5W$ – $2.3W$ . With the upstream shear layer attaching to near the leading edge of the downstream body, a strong vortex is produced within the gap, resonating at a constant Strouhal number based on the gap length. Although the vortex pair downstream of the second body resembles the vortices seen in the bistable regime, they behave differently. The vortex shedding frequency in the bistable region is associated with the span-wise separation of the vortex cores, while in the locked in region, oscillation occurring in the gap is the triggering mechanism for shedding from the downstream body. Therefore, the shedding frequency from the second body locks in with the resonance of the cavity. Over this range, the drag of the front cube almost reaches a plateau, while the drag of the rear cube still increases gradually.
3. Quasi-isolated regime: This regime is characterised by the large gap separation and a single shedding frequency occurring in the gap and downstream of the second body. The Strouhal number based on width increases gradually with the growth of gap size until it reaches the isolated body value. It is found that the shear layer separating from the leading edge of the first body no longer attaches to the second body. The vortices shedding from the first body triggers shedding from the second. This process synchronises the shedding between the first gap and the downstream wake. With further increases in gap size, the mutual interaction between the gap flow and the wake decreases. Eventually at a sufficiently large gap, vortex shedding is completely asynchronous. At a gap size of approximately  $6W$ , the drag on both bodies has reached a constant value experienced by an isolated body.

### 1.4. Double-stacked wagon in freestream

Characterisation of an individual double-stacked wagon in free-stream has been conducted by Li et al. (2015). They confirmed that the separated shear layers originating from the leading-edge corners reattached before reaching half of a wagon length. This leading-edge recirculation region consisted of three recirculation bubbles, as inferred from surface-flow visualisation. The overall surface-flow structure strongly resembles that of a surface-mounted cube subjected to a thick floor boundary layer (Castro and Robins, 1977). Additionally, an out-of-phase shedding from the sides of the wagon was identified in the wake, with a shedding frequency of  $St_w = 0.195$ . No characterisation of the flow field was made in proximity to other wagons.

1.5. Aim

It is known that single-stacked wagons and other bluff bodies experience aerodynamic drag as a function of separation distance or gap size, arising from changes to the flow topology. While there have been direct force measurement studies on the effect of gap size for train wagons, there are no detailed experiments that study of flow topology for varying gap sizes in the past literature. Of those force measurement studies conducted, the number of different gap sizes tested are limited.

Some parallels can be drawn from the flow topology over fundamental objects, such as surface mounted cubes in tandem, but none adequately reflects the geometric aspect ratio of container wagons. Additionally, as those studies are often targeted at wind engineering applications, cubes are typically surface mounted with no ground clearance, and Reynolds number is of an order lower than those presented in the current study.

This paper presents surface pressure measurements, surface visualisations, and flow-regime velocity measurements of a simplified double-stacked container wagon that is subjected to a varying combination of upstream (front) and downstream (rear) gap sizes,  $G_f$  and  $G_r$ , respectively.

It is expected that an isolated wagon will behave similarly to that of a surface-mounted cube when shear-layer reattachment occurs. In a tandem formation, due to this shear-layer reattachment, little similarity is expected between the flow state of wagons and surface-mounted cubes in tandem. The “bi-stable” and “locked-in” regimes discussed above rely on the interaction of the leading-edge shear-layer with the trailing edge, and the leading edge of the downstream cube, respectively. This will not happen for a wagon as the shear layers interacting with the downstream wagon originate from the trailing edge of the upstream wagon.

From past literature we know that the drag of a wagon will increase with an increase in both  $G_f$  and  $G_r$ . However, the question is how will varying  $G_f$  feed downstream and varying  $G_r$  feed back upstream? It is theorised that due to the length of the wagon,  $G_r$  is not likely to have a significant impact on the upstream pressure distribution. However, with a larger  $G_f$ , it is believed that a thicker boundary layer will be induced on the top and side surfaces, increasing the rear pressure and lowering the drag.

Ultimately, the purpose of detailing the flow characteristics of a wagon is to be able to estimate the pressure drag of an entire train through the summation of contributions from its individual wagons. Drag comparisons of a series of differently loaded trains will be performed to gain an appreciation of the loading configuration's impact on drag. It

seems obvious that drag will be reduced by reducing both the size and the number of gaps within the train, but whether reducing the number or the size of the gap is more important is still unclear.

2. Methodology

The experiments were conducted in the Monash University 450 kW closed-circuit wind tunnel. The wind tunnel had a test section of  $16 \times 2 \times 2 \text{ (m)}^3 (L \times W \times H)$ . Testing was conducted at 1:14.6 scale, with a flow velocity of  $\approx 30 \text{ m/s}$ , corresponding to a Reynolds number based on wagon width of  $Re_w = 0.3 \times 10^6$ . The free-stream turbulence intensity was approximately 1%, and the tunnel blockage was 2.4%.

A model representative of a 14.6 m (48 ft), double-stacked container wagon with dimensions  $L = 1000 \text{ mm}$ ,  $W = 171 \text{ mm}$ , and  $H = 438 \text{ mm}$  was employed. The model was placed above a false floor with a ground clearance of 28 mm, equivalent to the radius of a full-scale 410 mm wheel (32 inch). The wagon dimensions were based on a commonly sized wagon. The wagon was modelled using rectangular prisms; all extra features such as panel ribbing and under-body bogies were omitted.

The main setup consists of seven wagons aligned longitudinally, shown in Fig. 1. Excluding the leading wagon, each wagon's geometry was identical to the test wagon. While the leading wagon's overall dimension was the same as the rest, its nose was rounded to be similar to that of an Ahmed body (Ahmed, 1983) to limit front-edge flow separation. All instrumentation was connected on the test wagon, which was placed in the fourth position. Furthermore, all additional inter-wagon gaps were covered up in order to limit controlling variables to  $G_f$  and  $G_r$ , by preventing interaction between the front gap and upstream wagon gaps. While there were initial concerns that this may have over simplified the model, making it less representative. Testing the model with the smaller inter-wagon gaps covered and uncovered had yielded pressure drag coefficients with very minor differences, see Figs. 2 and 3. Both  $G_f$  and  $G_r$  were incrementally changed through 7 sizes each, resulting in a total of 49 different gap-size combinations. Additionally, the test wagon was also tested in free-stream by itself, the results of which are described in more detail in Li et al. (2015).

Other than the middle test wagon, all other wagons were not instrumented and were intended to limit the effect that shortening the train (by increasing  $G_f$ ) would have on the boundary layer on the wagon surface at the rear of the lead wagon. While it would be ideal to have more upstream and downstream dummy wagons, there was a limitation due to test section sizing and the growth of the floor boundary layer. This current setup results in a floor boundary-layer profile with properties

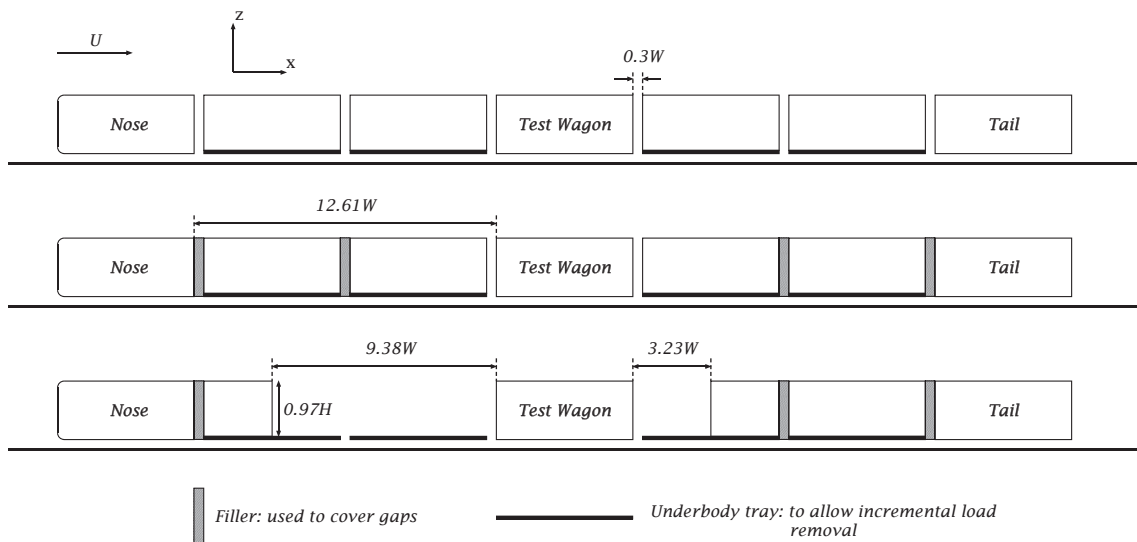


Fig. 1. Experimental setup.

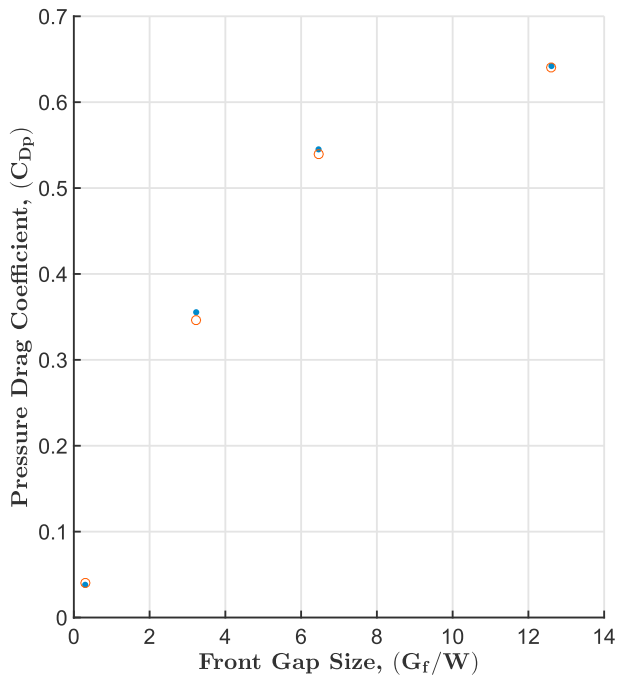


Fig. 2. Pressure drag coefficient with varying front gap sizes, rear gap sizes were kept constant at  $G_r = 0.3W$ . ● - (Inter-wagon gaps covered). ○ - (Inter-wagon gaps uncovered).

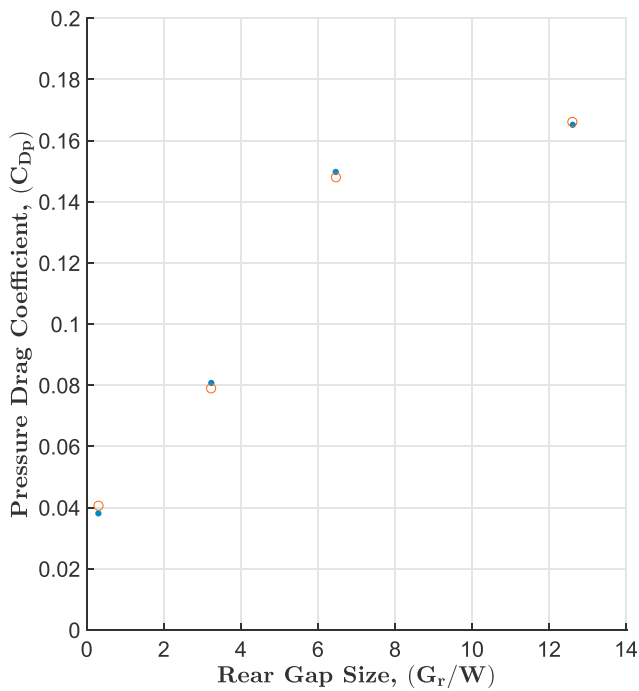


Fig. 3. Pressure drag coefficient with varying rear gap sizes, front gap sizes were kept constant at  $G_f = 0.3W$ . ● - (Inter-wagon gaps covered). ○ - (Inter-wagon gaps uncovered).

shown in Table 1, measured at the front face position of the test wagon. As (Li et al., 2015) illustrated through reducing the displacement thickness by 47% that the qualitative and quantitative changes in surface pressure and the final drag variations were minimal, no further reduction in the floor boundary layer thickness was pursued.

Surface pressure was measured on the “test wagon” using a total of 478 pressure taps, with 117, 121, 120 and 120 taps situated on the front, rear, top, and side surfaces, respectively. On the top and side surfaces, the taps were distributed along the centrelines of each surface. Fig. 4 displays the tap configuration employed for the front and rear surfaces. At a small rear gap size,  $G_f = 0.3W$ , a localised high-pressure node was measured by the rear tap indicated in blue. The 4 red taps surrounding the blue tap were additional taps added to help resolve this localised high-pressure region. Mean and fluctuating pressures were measured using two 64 channel Turbulent Flow Instrumentation dynamic pressure measuring systems (DPMS). Measurements were taken for a sampling time of 60 s at a sampling rate of 1000 Hz. PVC tubing of internal diameter 1.5 mm and length 1750 mm connects each tap to a corresponding transducer. To account for magnitude and phase distortion in the tube length the time dependent pressure is transformed into the frequency domain and a tubing correction transfer function applied, using the method described by Bergh and Tijdeman (Bergh and Tijdeman). The set-up adopted ensured that the frequency amplitude stays above 50% over the sampling frequency range.

The total and static pressure, measured from an upstream pitot-static tube, were corrected to the position equivalent to the test wagon's top-surface leading edge; these were used as reference values for all further pressure measurements.

Mean planar velocity fields in a number of vertical XZ planes, as displayed by Fig. 5, were measured using a cobra probe. The cobra probe is a four-holed pressure probe developed by turbulent flow instrumentation (TFI). It can measure three velocity components in a flow with an acceptance cone angle of 45°. It measures a velocity up to 50 m/s, and has a frequency response up to 2000 Hz. The cobra probes were traversed through the spatial plane using two mechanical traverses, one moving in the X direction, the other in the Z direction.

Surface-flow visualisation was conducted on the top and side surfaces of the test wagon using Kaolin china clay mixed with kerosene and fluorescent dye. The final images obtained were enhanced with UV light. When performing flow visualisation on the side surface, to prevent gravity from influencing the surface flow patterns, the train was mounted on its side on the wind tunnel sidewall.

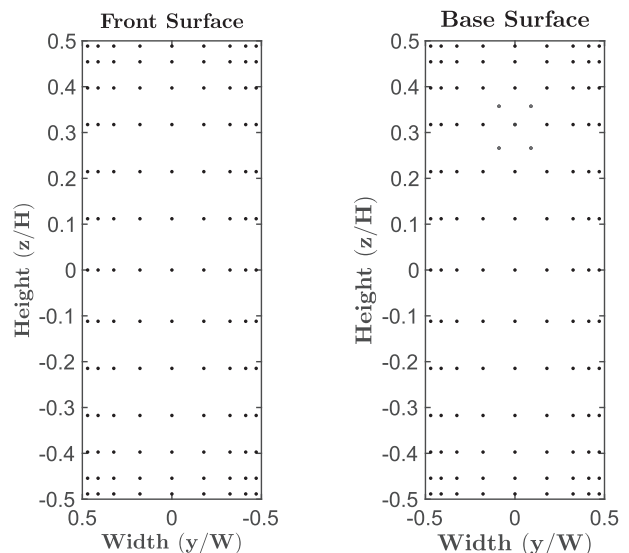


Fig. 4. Front and rear surface pressure tap locations.

Table 1

False-floor boundary layer properties, where  $\delta$  is the boundary layer thickness,  $\delta^*$  is the displacement thickness, and  $\theta$  is the momentum thickness.

$\delta/H$	$\delta^*/H$	$\theta/H$
0.46	0.036	0.031

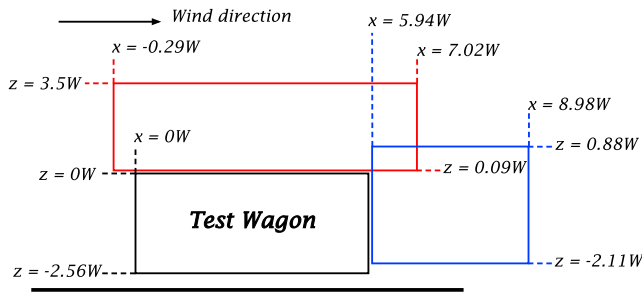


Fig. 5. XZ plane sweep conducted with the cobra probe. The red plane was used for  $G_f = 0.3W, 9.38W$  and  $G_r = 3.23W, 9.38W$ , and the blue plane for  $G_f = 0.3W, 9.38W$  and  $G_r = 3.23W$ . (For interpretation of the references to colour in this figure legend, the reader is referred to the web version of this article.)

### 3. Results and discussion

#### 3.1. Reynolds number sensitivity

The Reynolds number sensitivity of the model setup was assessed for both an isolated wagon in free-stream and a wagon within the full train setup under the minimum upstream and downstream gap size of  $0.3W$ , see Table 2. It was concluded that the sensitivity to Reynolds number is low. This is expected as the test wagon itself is a bluff body with clear separation points. Although the nose of the train had rounded leading edge, the train's nose was a considerable distance upstream of the test wagon. As such, any change in flow over the nose with Reynolds number had little effect on the downstream test wagon when  $Re > 0.1 \times 10^6$ . Similarly, Castro and Robins (1977) have found that when the Reynolds number for a surface-mounted cube is above  $Re = 3 \times 10^4$ , the shear layer is turbulent from the leading edge and good Reynolds number independence is achieved.

#### 3.2. Drag on a wagon as a function of $G_f$ and $G_r$

The pressure drag coefficient ( $C_{Dp}$ ) is determined from pressure measurements. The pressure is integrated over the front and rear surfaces to give an area-averaged pressure coefficient ( $C_p$ ). The difference between the front-surface pressure coefficient ( $C_{pfront}$ ) and rear-surface pressure coefficient ( $C_{prear}$ ) then gives the pressure drag coefficient of the wagon ( $C_{Dp}$ ).

$$C_{Dp} = C_{pfront} - C_{prear} \tag{1}$$

The pressure drag coefficient of a double-stacked wagon isolated in free-stream is found to be  $C_{Dp} = 0.94$ . Comparing to previous studies: Osth and Krajnovic (Östh and Krajnović, 2014) obtained a drag coefficient of 0.904 for a single-stacked wagon; Hammit (Hammit, 1976) reported a drag coefficient of 0.8 at Reynolds number of  $10^6$  for a single-stacked wagon with smooth under-carriage; and Peters (1993) found a drag coefficient of 0.9 for a 1:3-scaled container wagon with detailed geometry. Our measurements of a double-stacked container are slightly higher than these single-wagon studies, however given the differences in model geometries and experimental set-ups our results are within the expected range.

For tests with wagons in proximity to the test wagon, a maximum drag coefficient of 0.77 occurs for the maximum gap size of  $G_f = 12.61W$  and  $G_r = 12.61W$ , less than the  $C_{Dp} = 0.94$  measured for the single wagon

Table 2  
Reynolds number sensitivity of the test wagon in isolation and within a full train setup.

Reynolds Number ( $\times 10^6$ )	0.052	0.119	0.246	0.322	0.352	0.397
$C_{Dp}$ of the isolated test wagon	0.95	0.94	0.95	0.95	0.95	0.95
$C_{Dp}$ of the test wagon in baseline configuration	0.01	0.04	0.05	0.05	0.05	0.05

case. It is expected that further increases in gap size  $G_f$  and  $G_r$  may see the wagon's  $C_{Dp}$  increase slightly. However, there is a difference in the setup between the two cases; in this case there are flat cars upstream and downstream of the test wagon, unlike for the isolated wagon case. The minimum drag coefficient was measured at  $C_{Dp} = 0.026$ , which occurs for the combination of minimum front and rear gaps of  $G_f = 0.3W$  and  $G_r = 0.3W$ . Importantly, the worst-case configuration has a drag coefficient almost 29.6 times higher than the best case, which at full scale at 100 km/h is equivalent to an aerodynamic power difference of 150 kW per wagon.

The changes in pressure drag coefficient for the various  $G_f$  and  $G_r$  combinations are shown in Fig. 6 and Table 3. These data highlight a number of important features. First, the dominant effect on drag is the front-gap size. It is evident the rate of drag growth as a result of an increase in  $G_f$  is significantly greater than that caused by an increase in  $G_r$ . Second, an increase in drag coefficient with increasing rear gap is apparent for all front gap sizes, despite this being a secondary effect. Third, the highest rate of change of drag coefficient observed between any of the two  $G_f$  sizes that has been measured occurs over the range  $1.77W$ – $3.23W$ . This corresponds to a flow regime change within the gap, as will be shown later. This suggests the greatest opportunity for drag savings (per unit length) comes from reducing gap spacing in this region.

It then follows to consider the relative contribution of the front and rear pressure to these changes in drag. Table 4 shows the front-surface pressure variation, expressed as a pressure coefficient change from the minimum gap spacing ( $G_f = G_r = 0.3W$ ). Note that this is presented in a tabular form as a figure is unable to clearly depict the small changes in the pressure. Fig. 7 shows the variation of rear pressure coefficient for constant  $G_r$  and varying  $G_f$ . It is clear that the primary source of the changes in drag coefficient caused by gap changes are the variations to the pressure coefficient of the surfaces nearest the relevant gap. That is, the change in drag associated with an increase in front gap is attributable to a change in front-surface pressure, and a change in drag associated with an increase in rear gap is caused by a decrease in rear pressure. No discernible change in pressure on the front surface is caused by a change in  $G_r$ , that is, the rear condition does not propagate to the front of the wagon. However, an increase in  $G_f$  at a constant  $G_r$  will induce a small pressure drop on the rear surface, which typically amounts to 3% or less in overall drag. This appears counter-intuitive as we expect a larger boundary layer along the sides and roof of the wagons and therefore increased rear pressure; this will be further discussed later (Rowe et al., 2001).

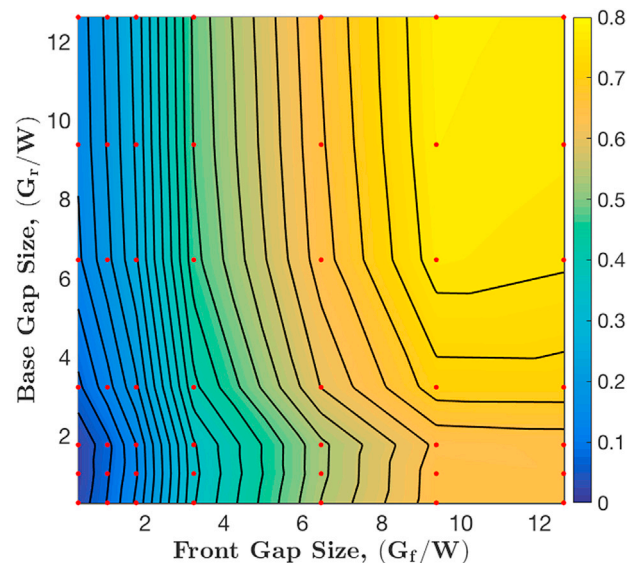


Fig. 6. Contour plot of pressure drag coefficient ( $C_{Dp}$ ) with respect to varying combinations of front ( $G_f$ ) and rear ( $G_r$ ) gap sizes.

**Table 3**  
Variation in drag coefficients for different front and rear gaps.

	0.3W	12.61W
0.3W	0.026	0.64
12.61W	0.15	0.77

By applying the front and rear pressure for matching gap sizes, it is possible to estimate the drag coefficient of a specific gap size (this is because the effect of front gap on rear gap, and vice versa is secondary). Here we use the average of all  $C_{pfront}$  (various rear gaps) to determine the  $C_{pfront}$  for each front gap. We also determine the average of all the  $C_{prear}$  (various front gaps) for each rear gap. We can then plot the drag ( $C_{pfront} - C_{prear}$ ) as a function of gap size, refer to Fig. 8. Again, this highlights an increase in drag for increasing gap size, with the highest gradient occurring in the range 1.77W–3.23W. It also provides a basic method for estimating drag from a gap and thereby summing individual drag contributions over the train length to produce an overall drag coefficient. Given the relative constancy of the opposing pressure coefficients with front and rear gap sizes discussed above, this approach has an implicit uncertainty of approximately 2%.

### 3.3. Steady state analysis of front and rear surfaces

#### 3.3.1. Single wagon in free-stream

To understand the cause of the changes to surface pressure, we consider the time-averaged front/rear surface-pressure distributions. The front and rear pressure distributions of the isolated double-stacked wagon in free-stream are displayed in Fig. 9. Similar to the results of Castro and Robin for a surface-mounted cube (Castro and Robins, 1977), the middle of the wagon's front surface exhibits a region of high stagnation pressure. Pressure then drops towards all edges of the surface as air flows around the corner.

The rear surface exhibits a region of low pressure, the magnitude of the  $C_p$  is comparable to the result for a surface-mounted cube under a thick floor boundary layer, where  $\delta = 10H$ . This is due to the leading-edge shear layer reattaching onto the surface of the wagon before reaching the trailing edge. The rear surface broadly displays three pressure regions seen as bands of different magnitude, with the lowest pressure region closest to the ground. This kind of distribution is seen in many square back flows and the pressure layout is due to two vertically stacked vortices in the time-averaged flow, with the lower vortex closer to the wagon surface, as illustrated by Osth et al. (Östh and Krajnović, 2014).

Fig. 10 displays the corresponding standard deviation of the  $C_p$  on the front and rear surface. It can be seen that the highest magnitude pressure fluctuations on the front surface are towards the bottom and associated with the oncoming boundary layer. The highest magnitude fluctuations occur on the rear at  $Z \approx -0.2$ , in the stagnation region between the two time-averaged vortices. Peaks in the standard deviation are also seen at the approximate mid-height, possibly associated with shedding from the wagon sides.

#### 3.3.2. Multiple wagons

The front/rear surface pressure distributions that yielded the pressure drag coefficients are presented in Fig. 11. It is evident that as  $G_f$  and  $G_r$

**Table 4**  
Front surface's  $C_p$  variation with respect to change in  $G_r$ .

	$G_r = 0.3W$	$G_r = 1.04W$	$G_r = 1.77W$	$G_r = 3.23W$	$G_r = 6.46W$	$G_r = 9.38W$	$G_r = 12.61W$
$G_f = 0.3W$	0.00	0.00	0.00	0.00	0.00	0.00	0.00
$G_f = 1.04W$	0.06	0.06	0.05	0.05	0.06	0.06	0.06
$G_f = 1.77W$	0.12	0.12	0.12	0.12	0.12	0.12	0.12
$G_f = 3.23W$	0.32	0.32	0.33	0.32	0.32	0.33	0.33
$G_f = 6.46W$	0.51	0.50	0.50	0.51	0.51	0.51	0.51
$G_f = 9.38W$	0.61	0.61	0.60	0.61	0.61	0.61	0.61
$G_f = 12.61W$	0.61	0.61	0.61	0.61	0.61	0.61	0.61

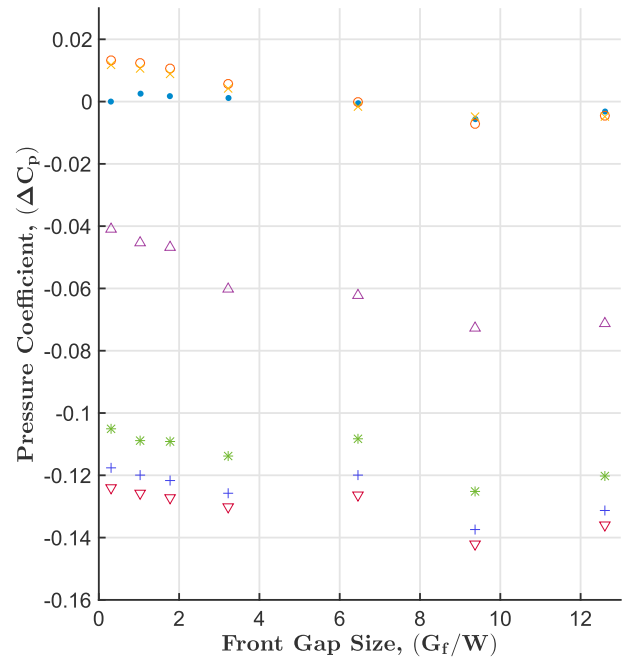


**Fig. 7.** Rear surface  $C_p$  variation with respect to change in  $G_f$ . ● - ( $G_r = 0.3W$ ). ○ - ( $G_r = 1.04W$ ). × - ( $G_r = 1.77W$ ). △ - ( $G_r = 3.23W$ ). \* - ( $G_r = 6.46W$ ). + - ( $G_r = 9.38W$ ). ▽ - ( $G_r = 12.61W$ ).

increase, the surface pressure contours gradually tends towards those of an isolated wagon in free-stream. The pressure on the front surface is seen to only be affected by the change in ( $G_f$ ). However, on the rear surface, pressure distribution is directly influenced by  $G_r$  and also affected by  $G_f$  but to a lesser extent. For a constant  $G_r$ , with an increase in  $G_f$ , the rear pressure drops, increasing the suction force on the rear surface, as was seen previously.

At  $G_f = 0.3W$  the front surface exhibits an overall uniform low pressure, except for the edges where there are signs of positive pressure, indicating a slight impingement of the upstream shear layer. Osth et al (Östh and Krajnović, 2014). illustrated that for multiple wagons in proximity, there are two counter-rotating vortices within a gap size of 0.5W, shielding the separating shear layers from the upstream wagon and transferring them across the gap where they re-attach on the roof and side of the container on the next wagon.

A slight increase of front gap to  $G_f = 1.04W$  sees more impingement of flow on the top and the upper region of the side edges; this is reflected by higher pressure in the corresponding region. There are still concentrations of low pressure just below the vertical halfway point. These low-pressure regions are organised in vertical bands, with a thin band of higher pressure in the middle. This is speculated to be caused by the two counter-rotating vortices mentioned above. The same is seen for  $G_f = 1.77W$ , however the low pressure region is seen to have shifted further downwards.

A regime change is observed between  $G_f = 1.77W$  and  $G_f = 3.23W$ : the pressures are higher and become more uniform over the front surface.

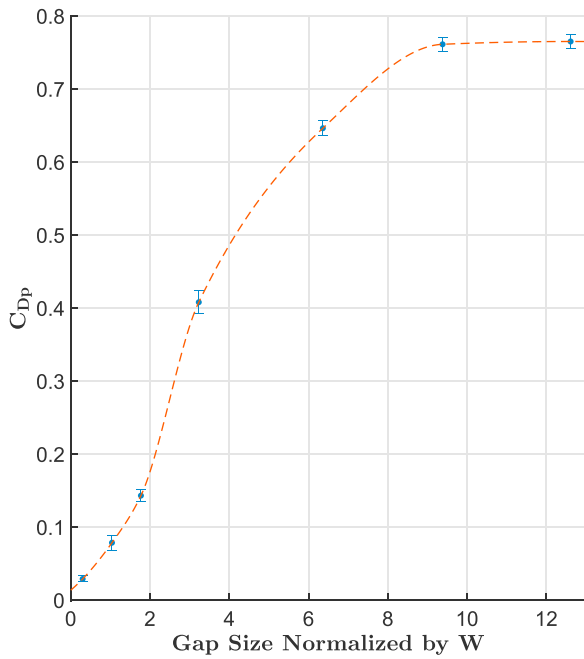


Fig. 8. Estimated drag coefficient of a gap size, where  $G_f = G_r$ .

The pressure contours now reflects that of a wagon isolated in free-stream. Most importantly, this regime change coincides with the highest rate of drag increase seen in Fig. 6. Further enlargement of  $G_f$  sees an increase in the magnitude of the pressure on the front surface, but will no longer alter the general nature of the contour pattern.

The regime shift between  $G_f = 1.77W$  and  $3.23W$  reflects the change between the upstream shear layer impinging on the leading edges of the downstream wagon's face versus full flow impingement on the entire downstream wagon's face. This is analogous to the shift between the "locked in regime" and "quasi-isolated regime" of surface-mounted cubes in tandem. The difference here is that the upstream shear layer originates from the upstream wagon's trailing edge compared to the upstream cube's leading edge. For 3D cubes tested by Havel et al. (2001) and 3D cylinders studied by Sakamoto et al. (Sakamoto and Haniu, 1988), the drag increase for increasing  $G_f$  is observed to be close to linear between  $0W$  and  $4W$ ; no sudden acceleration in drag penalty is observed. However, it is interesting to point out that for 2D cylinders with a spacing between

$1.5W$  and  $2W$ , a sudden increase in drag was observed by Ricciardelli (1994) and Hangan and Vickery (1999).

Multiple distinct pressure regimes were also observed on the rear surface across different  $G_r$  ranges. An increase in  $G_f$  does not cause significant changes to the rear pressure regime, but does reduce the rear pressure. Starting at  $G_r = 0.3W$ , a localised high positive region of pressure surrounded by lower pressure is observed towards the top section of the surface. There is also a thin band of high pressure on the vertical centreline, just below this localised high-pressure node. It is theorised this pressure node and the high-pressure band below it is a result of flow impingement at the middle of the two counter-rotating vortices.

At  $G_r = 1.04W$ , the pressure distribution has three bands, a band of lowest pressure is apparent at the top, with an immediate band of high positive pressure just below, and towards the bottom is another band of low pressure. Again, this appears to be consistent with the flow structure consisting of upper and lower counter-rotating vortices, with flow attachment occurring on the rear surface in between the two vortices, resulting in the band of positive pressure.

For a further increase in gap size to  $G_r = 1.77W$ , the lowest pressure band at the top remains present with an increase in pressure immediately below it. However, the bottom low-pressure band has disappeared, and pressure continues to rise as the position shifts downward, reaching the maximum near the bottom. A plausible explanation is that the lower of the two vortices shifts downstream away from the surface, leaving the upper vortex to impinge against the rear.

From  $G_r = 3.23W$  and onwards, the surface exhibits a three-band pressure contour pattern, with a relatively high-pressure region in the middle sandwiched by a low pressure on top, and an even lower pressure region at the bottom. From this point onwards, the rear pressure contours resemble that of a wagon in free-stream. It is theorised that the bottom vortex now impinges on the rear, with the upper vortex further downstream.

Velocity measurements in the XZ centreplane, obtained with a cobra probe, are shown in Fig. 12 for two different  $G_f$ s for constant  $G_r$ . On each plot there are vectors indicating the direction of the flow, bounded by red dashed lines. All data not bound by the dashed lines and without vectors are in a region of high turbulence and reversed flow; the cobra probe is not able to accurately take the measurements under those conditions. Formally, this boundary is defined by the region where more than 20% of velocity vectors lies outside the 45-degree acceptance cone of the probe.

The solid red vertical line indicates the position of the rear surface. The trailing wagon's front face is located at  $9.38W$ . When the front gap

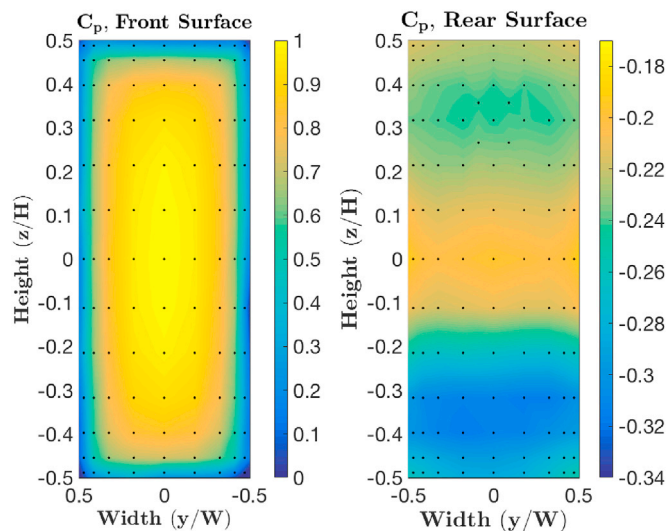


Fig. 9.  $C_p$  distribution on the front and rear surfaces of a double-stacked wagon in free-stream.

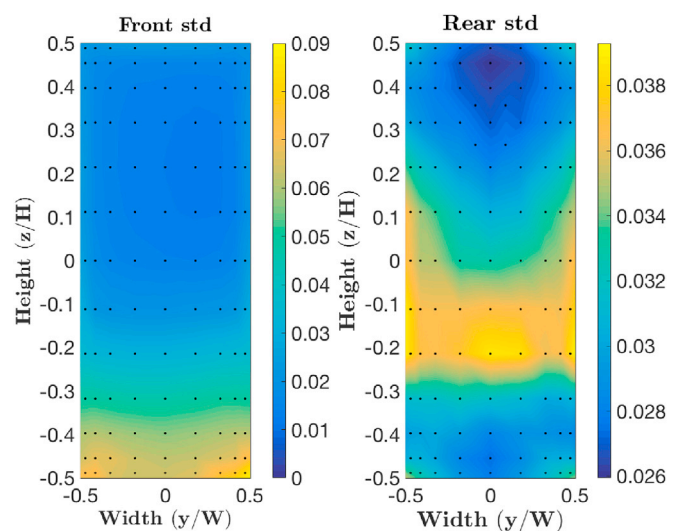


Fig. 10. Standard deviation of the  $C_p$  distribution on the front and rear surfaces of a double-stacked wagon in free-stream.

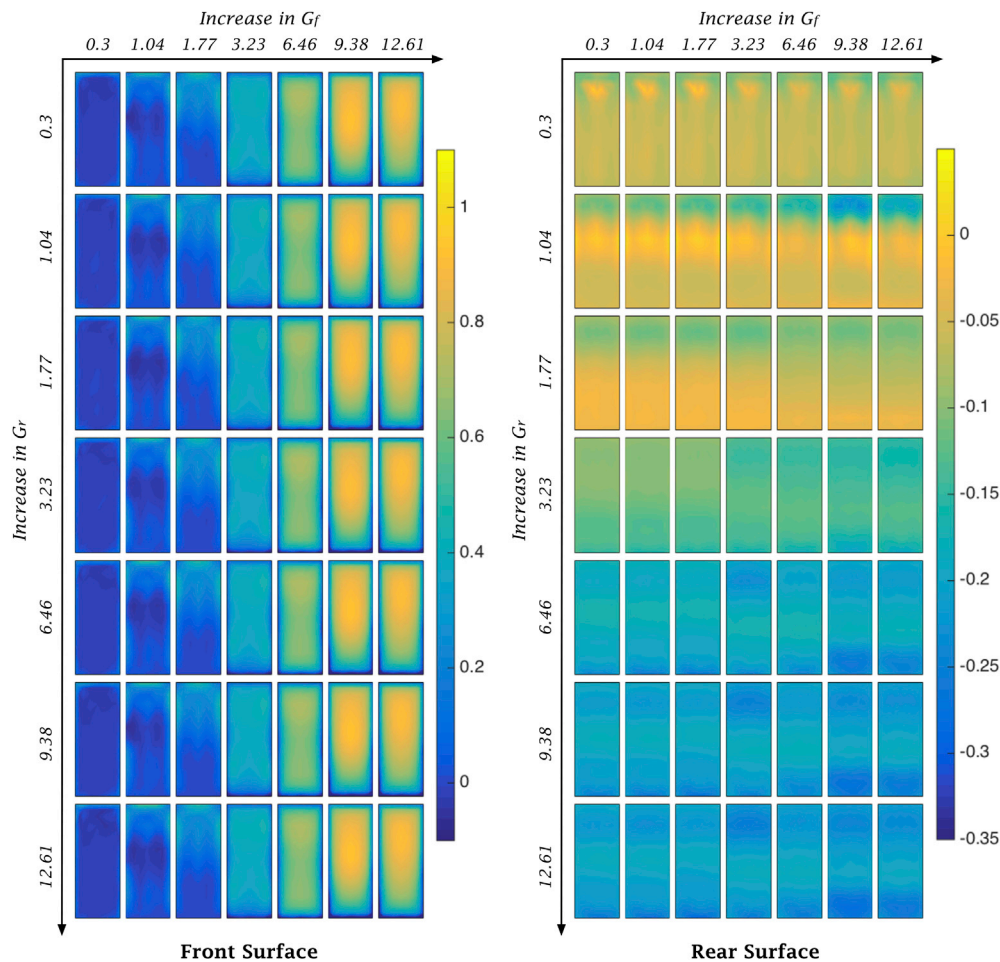


Fig. 11. The pressure coefficient ( $C_p$ ) distribution on the front and rear surfaces, presented for varying front ( $G_f$ ) and rear ( $G_r$ ) gap sizes.

size is increased from  $G_f = 0.3W$  to  $G_f = 9.38W$ , we can see that the relative size of the wake, indicated by the red boundary, has reduced. It is suspected that this contraction has forced the lower pressured core of the recirculating region upstream closer to the rear surface, resulting in a lower rear pressure.

### 3.4. Steady state analysis of top and side surfaces

The top and side surface flow visualisation of the single wagon is presented in Fig. 13, and an interpretation of the flow topology is shown in Fig. 14. It can be inferred that the separating shear layer rolls up into two small and one large recirculating bubbles. The subsequent reattachment lines R1 and R2 can be seen. This is similar to the recirculating structure proposed by Martinuzzi and Tropea (1993) on their surface-mounted cube experiments. In that case, there are two quasi-steady vortex cores on the sides, just behind the leading edges, impinging on the side surface and the floor. The same vortices are present on the wagon, displayed as V1 and V2 respectively. These two vortices are believed to be the nodes of a single rolled-up corner vortex, spanning the height of the wagon. Note that, compared to the cube, the position of both V1 and V2 is shifted upward, with V1 shifting from just above the mid-height position to just below the top edge, whilst V2 has moved from the floor onto the bottom edge of the wagon. Martinuzzi and Tropea (1993) also proposed the existence of two similar types of vortices on the top surface, just behind the leading edge. This vortex pair was not observed on the wagon. Despite this there is evidence of flow curvature occurring.

Osth and Krajnovic's (Östh and Krajnović, 2014) numerical simulation of a single-stacked container wagon in free-stream displayed a

recirculation bubble on the top surface. The recirculation bubble's length reported was  $1.75W$ . The recirculation bubble size in the current study, based on the distance between the leading edge and the position of R2 in the flow visualisation, is approximately  $2.28W$ .

The effects of the top and side surface flow features described above on the corresponding surface pressure distribution are depicted in Fig. 15. For reference, Castro and Robin's (Castro and Robins, 1977) surface-mounted cube and Osth et al.'s (Östh and Krajnović, 2014) single-stacked container wagon results are also plotted. The current wagon, that used by Osth et al., and the surface-mounted cube, have length-to-height ratios of  $L/W = 5.85$ ,  $5$ , and  $1$ , respectively. Osth et al.'s pressure profile displays very similar properties to those obtained for this current study, showing a low-pressure minimum followed by a pressure recovery indicative of reattachment. Therefore it may be argued that Osth et al.'s surface flow structure would be qualitatively similar to that of the current wagon. On the other hand, for the surface-mounted cube of Castro, only the cube under a relatively thick boundary layer experiences a pressure recovery similar to that of this wagon.

#### 3.4.1. Multiple wagon setup

Photographs of the top and side surface-flow visualisations obtained for varying gap sizes are shown in Fig. 16, with an interpretation of the cross-plane flow leading to the surface lines overlaid. The stream-wise position is labelled along the top edges. These images provide a qualitative description of the surface-flow topology along the surfaces of the wagon.

For  $G_f < 1.77W$ , the flow appears to bridge the gap and remains attached on both the top and side surfaces; however, the top and side surface pressure distributions show that there is separation at the leading

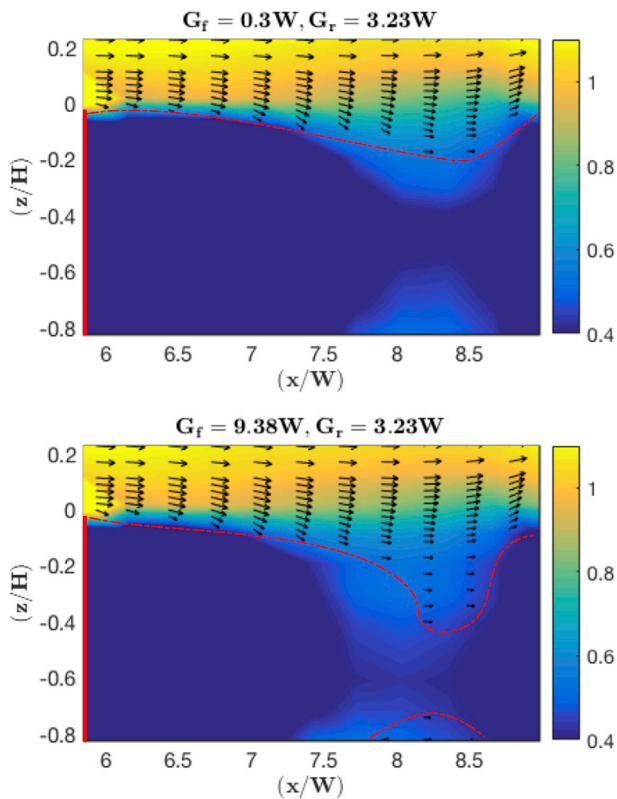


Fig. 12. XZ-plane velocity field vector plot. The color-bar indicates magnitude of velocity. (For interpretation of the references to colour in this figure legend, the reader is referred to the web version of this article.)

edge for  $G_f = 1.77W$ .

For a front gap of  $G_f = 3.23W$ , flow separates from the leading edge with a subsequent reattachment line just upstream of  $0.5W$ , labelled as  $R2$ . The reattachment line  $R1$  cannot be seen and it is unclear whether this is present or not. It may occur and be so close to the leading edge that it is not resolvable, or alternatively the associated flow structure may have insufficient momentum to overcome the viscosity of the applied fluid. An interpreted schematic of this case is displayed in Fig. 17. It is observed that some of the fluid pooling seen near the leading edge of the top surface is associated with the small surface discontinuity where the front face panel mates with the top surface.

For a front gap size of  $G_f = 6.46W$  and above, the general flow structure shows similarity to a single wagon in free-stream. The reattachment line  $R1$  appears on both the top and side surfaces, just slightly behind the leading edge. On the side surface, a vortex  $V2$  can be located towards the leading-edge and bottom-edge corner. Although flow curvature can be seen on the side surface on the top edge,  $V1$  was not observed.

A further increase in  $G_f$  shifts the position of the reattachment lines downstream,  $R2$  a lot more so than  $R1$ . The maximum reattachment length, defined as the furthest distance any point on  $R2$  is from the leading edge for each gap case, is plotted against  $G_f$  in Fig. 18. The growth in this reattachment length, and the relative distance between  $R1$  and  $R2$  reflects the growth in the size of the recirculation bubble as  $G_f$  increases. A change in  $G_r$  is not seen to have any impact on the reattachment length and position. An interpreted flow topology for the  $G_f = 9.38W$  and  $G_r = 0.3W$  case is displayed in Fig. 19.

By inspection of Figs. 20 and 21 it is evident that for increasing  $G_f$ , the surface-pressure and standard-deviation profiles along the top and sides of the wagon approach those of a single wagon in free-stream, as shown with the pressure distribution and flow topology.  $G_f$  has the dominant effect on the top/side surface pressure distribution. Increase in  $G_f$  enlarges the recirculation region and thereby delays the pressure recovery.

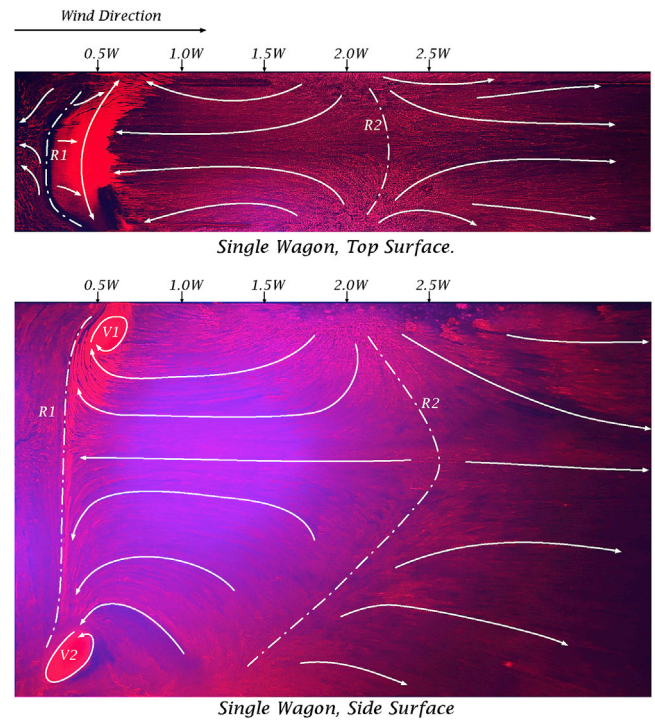


Fig. 13. Surface-flow visualisation produced by Kaolin china clay, enhanced using fluorescent dye and UV light.

The pressure recovery position can be seen to shift downstream with increase in  $G_f$ . The peak in standard deviation also shifts further downstream with larger  $G_f$ , and its position is always upstream of  $R2$ , likely associated with the intermittency of shear-layer reattachment.  $G_r$  in contrast is shown to have minimal impact on the overall pressure profile. A large jump from  $G_r = 0.3W$  to  $G_r = 9.38W$  only causes an average  $C_p$  drop of 0.14 and 0.12 at the rear-most pressure tap on the top and side surfaces, respectively.

The relative positions of reattachment lines  $R1$  and  $R2$  are represented as vertical yellow and purple dashed lines respectively. We note the position of reattachment line  $R2$  does not necessarily coincide with the maximum reattachment length defined earlier as pressure taps were only installed on the mid-line of the top/side surfaces. Thus the purple lines only depict the position of  $R2$  along the middle of the top/side surfaces.

The plots indicate that the position of  $R2$  generally occurs at a position prior to the top of the pressure recovery, i.e., the turning point of the curve.  $R1$  on the other hand, seems to coincide with the initial local minima on the standard deviation profile. Therefore, it is argued that  $R2$  exists immediately behind the leading edge for  $G_f = 1.77W$ , despite not being observed in the surface flow visualisation. According to this pattern  $R1$  may indeed not exist in both the  $G_f = 3.23W$  and  $G_f = 1.77W$  cases.

For a small frontal gap of  $G_f = 0.3$ , no separation is observed at the leading edge according to the velocity field measurements. However, a separated and recirculating region can be clearly seen by the cobra probe field measurement for the  $G_f = 9.38$  case shown in Fig. 22. This recirculation region coincides with the pressure minimum on the surface-pressure distribution shown in Fig. 20. The data with quality less than 80% is again bounded by the red dashed line, and it gives an approximate limit of the size of the recirculating region. The downstream boundary of the low quality region falls just short of  $1.5W$ , relatively close to the position of  $R2$  displayed by surface-flow visualisation, and the point of maximum surface pressure recovery presented in Fig. 20.

Boundary layer measurements were performed on the top surface of the wagon (Figs. 23 and 24) at four  $X$  locations,  $X = 0W, 1.75W, 2.92W, 5.85W$ , corresponding to the position of the leading edge, downstream

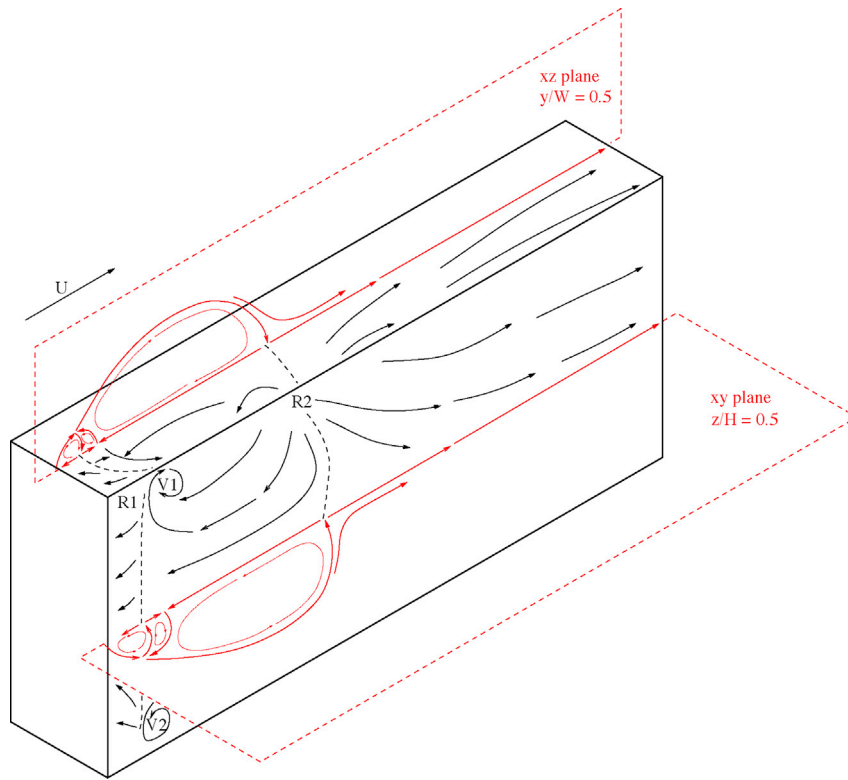


Fig. 14. Inferred flow structure of a single wagon in free-stream based on the surface-flow visualisation (Li et al., 2015).

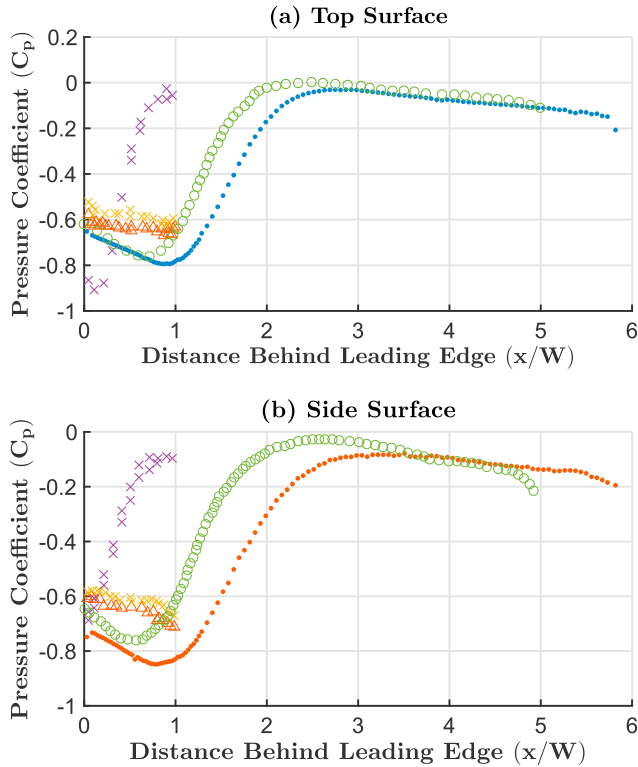


Fig. 15.  $C_p$  distribution on the top and side surfaces of a single wagon in freestream, including comparison with the data of Castro (Castro and Robins, 1977) and Osth et al. (Östh and Krajnović, 2014). (a) ● - Single Wagon, ( $\delta = 0.46H$ ). △ - Castro, false floor, ( $\delta = 0.025H$ ). × - Castro, tunnel floor, ( $\delta = 0.1H$ ). ○ - Castro, tunnel floor, ( $\delta = 10H$ ). ○ - Osth. (b) ● - Single Wagon, ( $\delta = 0.46H$ ). △ - Castro, false floor, ( $\delta = 0.025H$ ). × - Castro, tunnel floor, ( $\delta = 0.1H$ ). ○ - Castro, tunnel floor, ( $\delta = 10H$ ). ○ - Osth.

edge of recirculation bubble (for the  $G_f = 9.38W$  case), mid point of wagon, and the trailing edge, respectively.

At the leading edge, a larger  $G_f$  creates a boundary layer with greater velocity deficit towards the surface, but with lower turbulence intensity. The boundary-layer velocity deficit is further amplified by the presence of the recirculation bubble, additionally, turbulence intensity is greatly amplified. Moving further downstream, velocity recovery is observed, and turbulence intensity gradually lowers. At the trailing edge, the boundary layer profiles of the large front gap (e.g.  $G_f = 9.38W$ ) are very similar to those for the small front gap (e.g.  $G_f = 0.3W$ ), however with approximately double the turbulence intensity. It appears that the lower rear pressure induced by an increased front gap is associated with turbulence intensity and not shear in the boundary layer. Having a  $G_r = 9.38W$  in contrast to  $G_r = 0.3W$  is only seen to accelerate the boundary layer velocity towards the trailing edge of the wagon, creating a thinner boundary layer. Overall, it has negligible impact on the turbulence intensity profile of the boundary layer on the top surface.

These observations provide an explanation for the effect that  $G_f$  and  $G_r$  have on the rear pressure. A larger  $G_r$  will induce a thinner boundary layer at the trailing edge of the wagon. Rowe et al. (2001) have explained that a thinner boundary layer will have less diffused vorticity, therefore taking less time for circulation to be transferred across the wake to form an opposite vortex, thereby initiating the Karman like shedding process. It will subsequently mean a higher shedding frequency (this is documented in a later section) is achieved, with increased rate of fluid entrainment across the wake. These will result in a smaller wake and consequently a lower rear pressure.

Increasing the  $G_f$  is seen not to affect the boundary layer profile at the trailing edge, as the wagon is sufficiently long for this relaxation to occur. However, the turbulence intensity remains significantly higher due to the larger leading-edge separation. As is shown by Bearman et al. (Bearman and Morel, 1983), higher turbulence increases the entrainment and curvature of the shear layer, creating a smaller wake and lower rear pressure. This however, does not explain why larger  $G_f$  will reduce the wake shedding frequency, as will be shown in later section. It is theorised

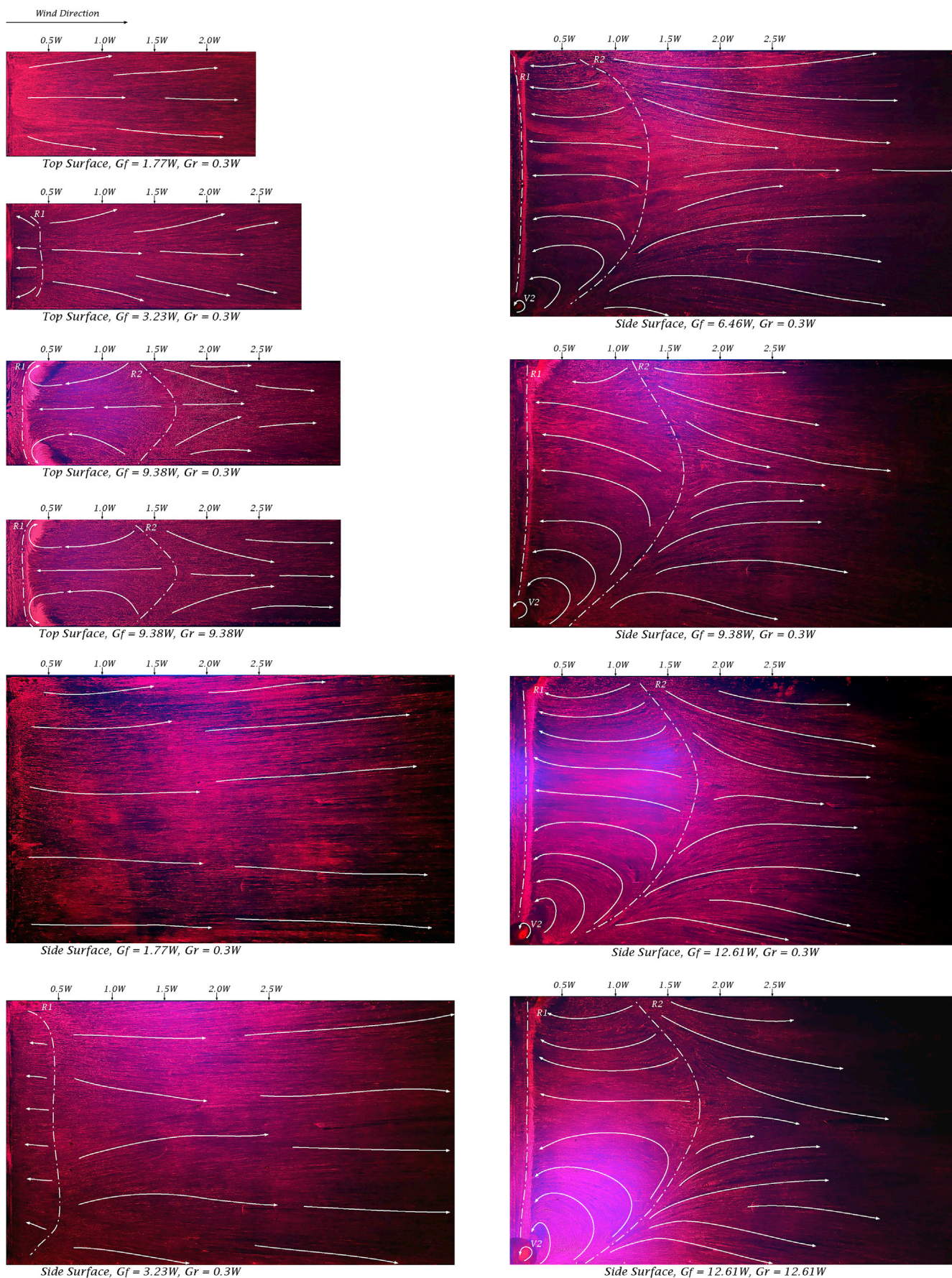


Fig. 16. Top and side surface flow visualisation using china clay enhanced with UV light.

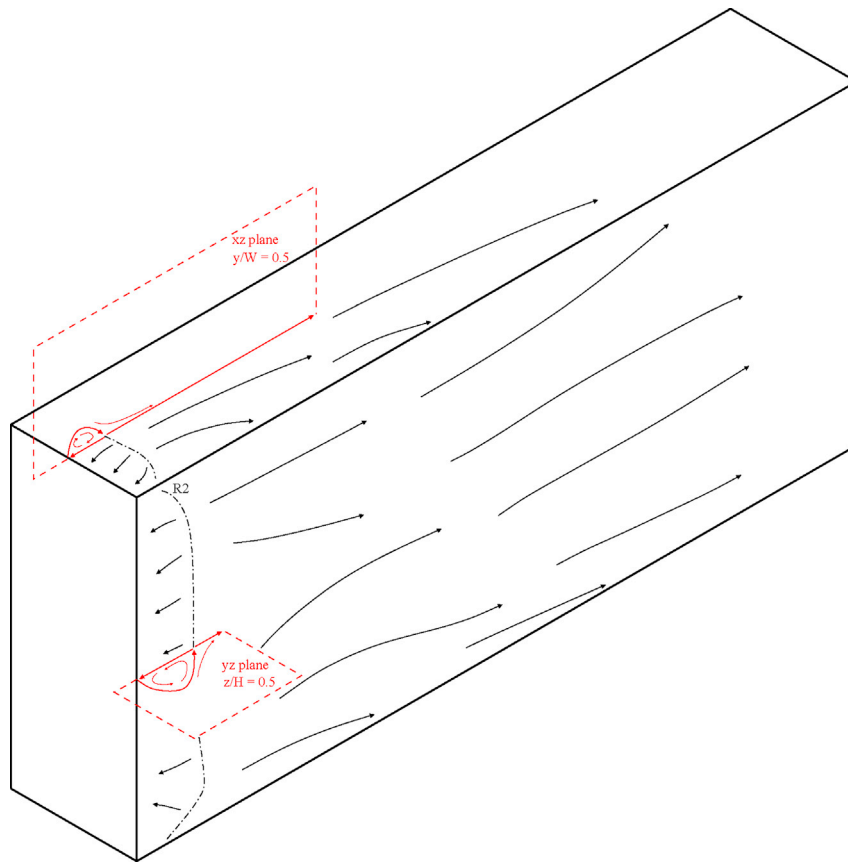


Fig. 17. Flow schematic for  $G_f = 3.23W$  and  $G_r = 0.3W$  interpreted from flow visualisation.

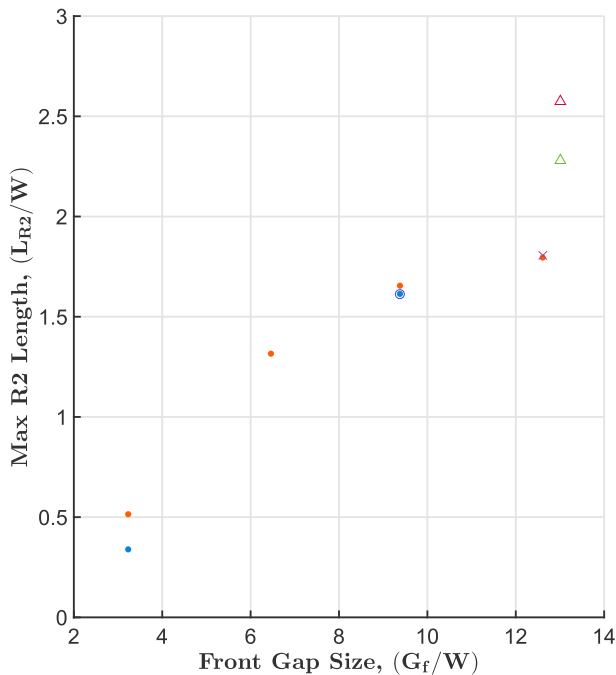


Fig. 18. Maximum reattachment length of R2 with respect to front gap size. ● - Top, ( $G_r = 0.3W$ ). ● - Side, ( $G_r = 0.3W$ ). ○ - Top, ( $G_r = 9.38W$ ). × - Side, ( $G_r = 9.38W$ ). △ - Top, Single Wagon. △ - Side, Single Wagon.

that on the side surface, the boundary layer may not have recovered as fully as the top surface does, resulting in a thicker boundary layer for a larger  $G_f$ . This will create a wider lateral wake and lower shedding frequency. Further testing will be required to confirm this.

### 3.5. Transient nature of the wake

Castro (1981) has shown that a surface-mounted prism of a longer ( $L/H \gg 1$ ) and wider ( $W/H \gg 1$ ) body will hinder the interaction of the lateral shear-layer pair, therefore deterring Karman-like shedding from occurring. Maull and Young (1973) have demonstrated how an increase in shear gradient promotes flow reattachment onto a surface, and the suppression of vortex shedding on a two-dimensional object. This behaviour is shown by Castro and Robin (Castro and Robins, 1977), where wake shedding wasn't observed for a boundary layer of  $\delta = 10H$ , but is detected for  $\delta = 0.025H$ . The wagon tested here had a length-to-height ratio of  $L/H = 2.28$  and width-to-height ratio of  $W/H = 0.39$ , it is also submerged in a floor boundary layer of  $\delta = 0.46H$ .

Power spectra of three side pressure taps are shown in Fig. 25. The resulting spectra show similarities to those observed on surfaces experiencing reattaching flow, such as a forward-facing step (Camussi et al., 2008; Cherry et al., 1984; Hudy et al., 2003). A highly fluctuating broadband region is observed towards the lower frequencies; Camussi et al. (2008) explain that this is indicative of the presence of large-scale oscillations within the shear layer, this is also reported by Hoarau et al. (2006). From the position of reattachment R2 and further downstream, a noticeable peak is observed at  $St_w = 0.19$ , corresponding to the wake shedding frequency, as will be shown later. This narrow-band peak is also observed by Camussi et al. (2008) for a forward-facing step. Higher frequencies are seen to have a power-law decay with an approximate exponent of  $-2$ , although, for the trailing-edge tap, the power-law decay exponent is closer to  $-1.5$ . This shows a tendency for the flow to recover towards an equilibrium turbulent boundary layer, represented by a power law exponent of  $-1$  (Leclercq et al., 2001).

Power-spectrum analysis for the rear surface reveals a general peak frequency with a Strouhal number based on width of  $St = 0.19$ . This signal amplitude is the greatest towards the side edges; its strength

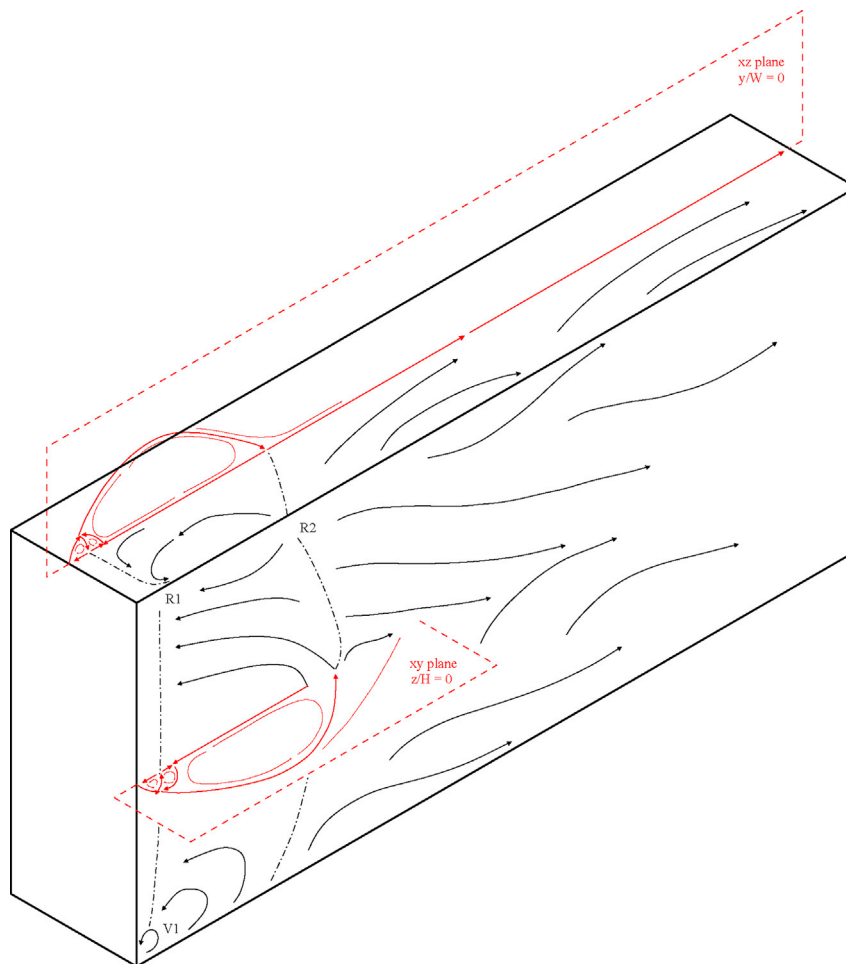


Fig. 19. Flow schematic for  $G_f = 9.38W$  and  $G_r = 0.3W$  interpreted from flow visualisation.

decreases on moving towards the middle vertical centreline. Fig. 26 presents a comparison of spectra between a pressure tap on the far right edge and one lying on the vertical centre line. The  $St_w = 0.19$  frequency is not observable on the vertical centreline. By taking account of the peak amplitude corresponding to this  $St = 0.19$  frequency at each tap position, a 2D representation of the power of this signal can be presented by Fig. 27 (left). The cross-spectrum between symmetrical taps about the vertical centreline outputs the relative phase angle between symmetrical taps, see Fig. 27 (right). The majority of taps pairs symmetrically positioned about the centreline are approximately  $180^\circ$  out of phase. Therefore, it can be confirmed that a left-right Karman-like shedding is present in the wake of the wagon. Note that thin sharp peaks at higher frequencies have been previously documented to be associated with wind tunnel noise.

For the multi-wagon setup, gap sizes above  $3.23W$  exhibit a dominant shedding signal. Tables 5–7 display the shedding signal detected by the front and rear surface pressure taps.

A second shedding signal can be detected when  $G_f \geq 3.23W$ , as presented in Table 7. This signal is the shedding frequency originating from the upstream gap; this can be confirmed by comparing it with the values in Table 5. The strength of this second signal is weak relative to the shedding signal originating from the downstream gap, making it difficult to detect. For  $(G_f = 3.23W, G_r = 1.04W)$  and  $(G_f = 6.46W, G_r = 1.04W)$ , the upstream shedding signal is not visible. For  $G_f = 3.23W$ , the second signal disappears after  $G_r > 3.23W$ ; this is because the frequency of this signal is so close to the shedding frequency from the rear gap, so it is not resolvable on the power spectrum.

Increasing  $G_f$  increases the rate of shedding within the front gap, as indicated by the increase in  $St_w$  from 0.19 to 0.27 in Table 5. Within the

rear gap, an increase in  $G_r$  acts to increase the shedding signal; this trend asymptotes at larger gap size, see Table 6. These increases in shedding frequency were expected as their mechanism has been explained in the previous section.

The rear gap size variation is shown to have no effect on the shedding frequency of the signal within the front gap. However, an increase in  $G_f$  will cause the shedding frequency in the rear gap to drop, this also tapers off at larger gap size. As discussed in the previous section, this is theorised to be caused by the thicker boundary layer at the trailing edge of the side surfaces, thereby creating a wider effective gap.

As hypothesised the “bistable” and “locked-in” shedding regimes found for surface-mounted cubes in tandem are not observed. The shear layer separating off the trailing edge of the wagon never reaches the trailing edge of the downstream wagon, and is therefore unable to create the “bistable” regime. The “locked-in” regime occurs for cubes when the leading-edge shear layer impinges on the leading edge of the downstream wagon. While this does occur for the trailing-edge shear layer of the wagon, it is likely that the wagon’s shear layer curvature is not great enough to allow the lateral shear layers to interact in such ways to create the locked-in regime.

### 3.6. Loading configuration simulation

As the underlying purpose of this research is to be able to estimate the drag of a train with any loading configuration, which could be used for optimising loading, in this section we estimate the drag on some trains with different loading configurations. The pressure drag of any 14.6 m (48 ft) double-stacked wagon can be calculated as the integrated pressure

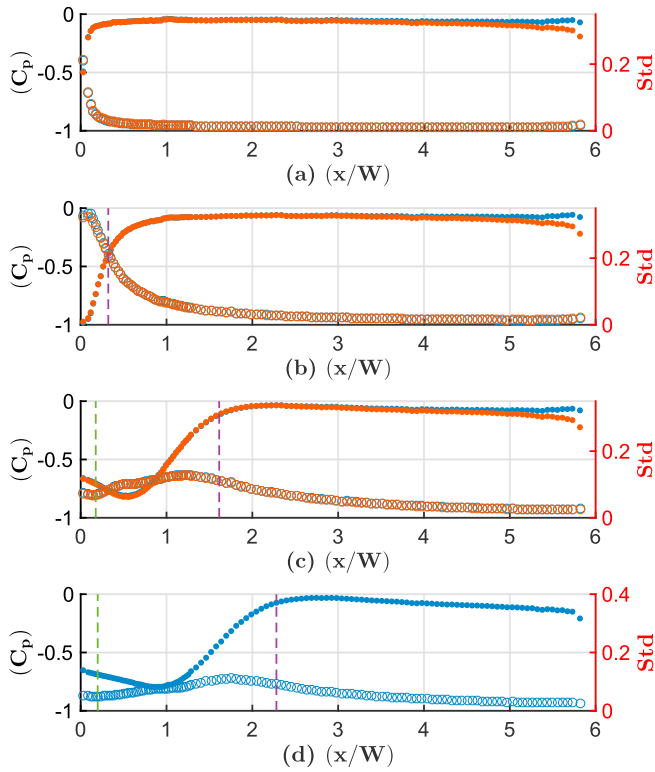


Fig. 20. Top surface  $C_p$  distribution as a function of normalised wagon length  $x/W$ . | - R1. | - R2. (a) ● -  $C_p$ , ( $G_f = 1.77W$ ,  $G_r = 0.3W$ ). ● -  $C_p$ , ( $G_f = 1.77W$ ,  $G_r = 9.38W$ ). ○ - Std, ( $G_f = 1.77W$ ,  $G_r = 0.3W$ ). ○ - Std, ( $G_f = 1.77W$ ,  $G_r = 9.38W$ ). (b) ● -  $C_p$ , ( $G_f = 3.23W$ ,  $G_r = 0.3W$ ). ● -  $C_p$ , ( $G_f = 3.23W$ ,  $G_r = 9.38W$ ). ○ - Std, ( $G_f = 3.23W$ ,  $G_r = 0.3W$ ). ○ - Std, ( $G_f = 3.23W$ ,  $G_r = 9.38W$ ). (c) ● -  $C_p$ , ( $G_f = 9.38W$ ,  $G_r = 0.3W$ ). ● -  $C_p$ , ( $G_f = 9.38W$ ,  $G_r = 9.38W$ ). ○ - Std, ( $G_f = 9.38W$ ,  $G_r = 0.3W$ ). ○ - Std, ( $G_f = 9.38W$ ,  $G_r = 9.38W$ ). (d) ● -  $C_p$ , (Single Wagon). ○ - Std, (Single Wagon).

difference between the front and rear  $C_p$ , as depicted by Equation (1). The total pressure drag coefficient for any section of the train can then be estimated as:

$$C_{DpTotal} = \sum_{i=wagon} C_{Dpi} \quad (2)$$

Estimations of the drag of 6 different loading configurations, normalised against the baseline drag, are shown in Fig. 28. It is confirmed that one should avoid having large gaps, however because the drag penalty plateaus for gap sizes greater than  $6.46W$ , one large gap is more favourable than multiple moderately sized gaps of the same total gap size. The benefit of reducing gap size is only significant once the gap size is reduced to below  $6.46W$ , remembering that the greatest potential drag reduction occurs between a gap size of  $1.77W$  and  $3.23W$ .

It must be re-iterated here that the purpose of above calculation isn't to calculate the exact drag value of a segment of the train for a specific loading configuration. It is to provide a comparison of drag between multiple possible loading configurations to assess which configuration will provide (near-)optimal drag reduction. For this purpose simplifications to the undercarriage geometry of the model is believed to be acceptable, as the geometry differences caused by adding containers are the main interest. For similar reasons, boundary-layer effects and the impact of wagon's position on its drag profile are not considered.

### 3.7. Measurement uncertainty

The two DPMS units used have measurement ranges of  $\pm 3$  and  $7$  kPa. The manufacturer stated accuracy at constant temperature of  $25^\circ\text{C}$  of each channel (transducer) is  $\pm 0.1\%$  of full scale for static measurements. However, in this study all pressure measurements are normalised by the

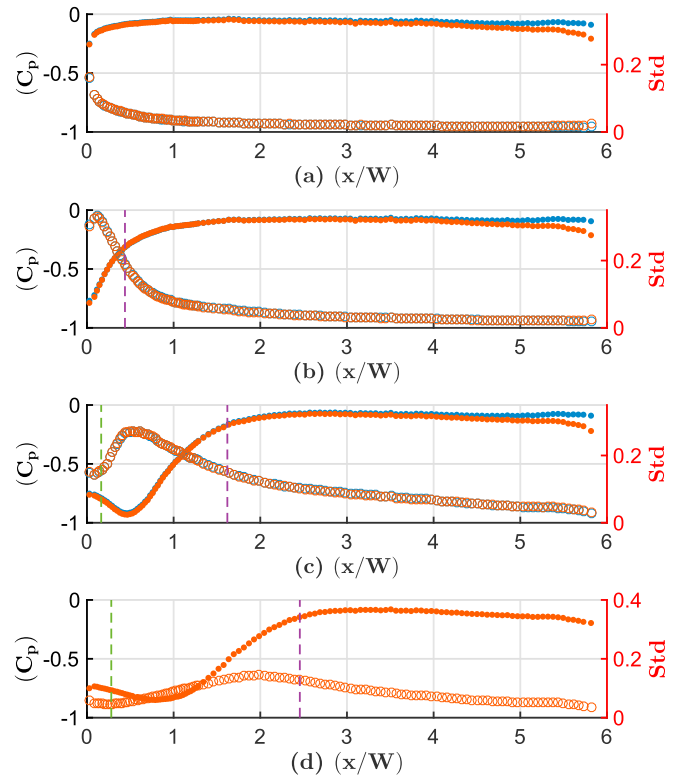


Fig. 21. Side surface  $C_p$  distribution as a function of normalised wagon length  $x/W$ . | - R1. | - R2. (a) ● -  $C_p$ , ( $G_f = 1.77W$ ,  $G_r = 0.3W$ ). ● -  $C_p$ , ( $G_f = 1.77W$ ,  $G_r = 9.38W$ ). ○ - Std, ( $G_f = 1.77W$ ,  $G_r = 0.3W$ ). ○ - Std, ( $G_f = 1.77W$ ,  $G_r = 9.38W$ ). (b) ● -  $C_p$ , ( $G_f = 3.23W$ ,  $G_r = 0.3W$ ). ● -  $C_p$ , ( $G_f = 3.23W$ ,  $G_r = 9.38W$ ). ○ - Std, ( $G_f = 3.23W$ ,  $G_r = 0.3W$ ). ○ - Std, ( $G_f = 3.23W$ ,  $G_r = 9.38W$ ). (c) ● -  $C_p$ , ( $G_f = 9.38W$ ,  $G_r = 0.3W$ ). ● -  $C_p$ , ( $G_f = 9.38W$ ,  $G_r = 9.38W$ ). ○ - Std, ( $G_f = 9.38W$ ,  $G_r = 0.3W$ ). ○ - Std, ( $G_f = 9.38W$ ,  $G_r = 9.38W$ ). (d) ● -  $C_p$ , (Single Wagon). ○ - Std, (Single Wagon).

dynamic pressure (see Equation (3)), as such, the uncertainty in the reported mean pressure coefficients ( $\xi_{Cp}$ ) is a function of the linearity of the individual channels (both the dynamic pressure and surface pressure transducers), the uncertainty of the calibration pressures and the use of an upstream pitot-static tube to infer the dynamic pressure at the model. The individual pressure transducers were simultaneously calibrated across ten points over the range of pressures measured in these experiments ( $\pm 1$  kPa), using a peristaltic pump to apply a static pressure and a Betz Manometer ( $\pm 0.1\%$ ) as the reference measurement device. These measurements were repeated five times for each channel to provide an estimate of static pressure uncertainty ( $\xi_p$ ), expressed as the average deviation from the expected value, giving  $\xi_p = \pm 0.4$  and  $\pm 1.6$  Pa for the  $\pm 3$  and  $7$  kPa DPMS units, respectively.

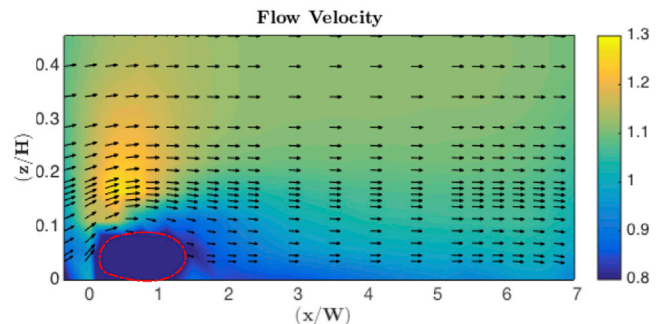


Fig. 22. Flow field above the wagon for  $G_f = 9.38W$  and  $G_r = 3.23W$ .

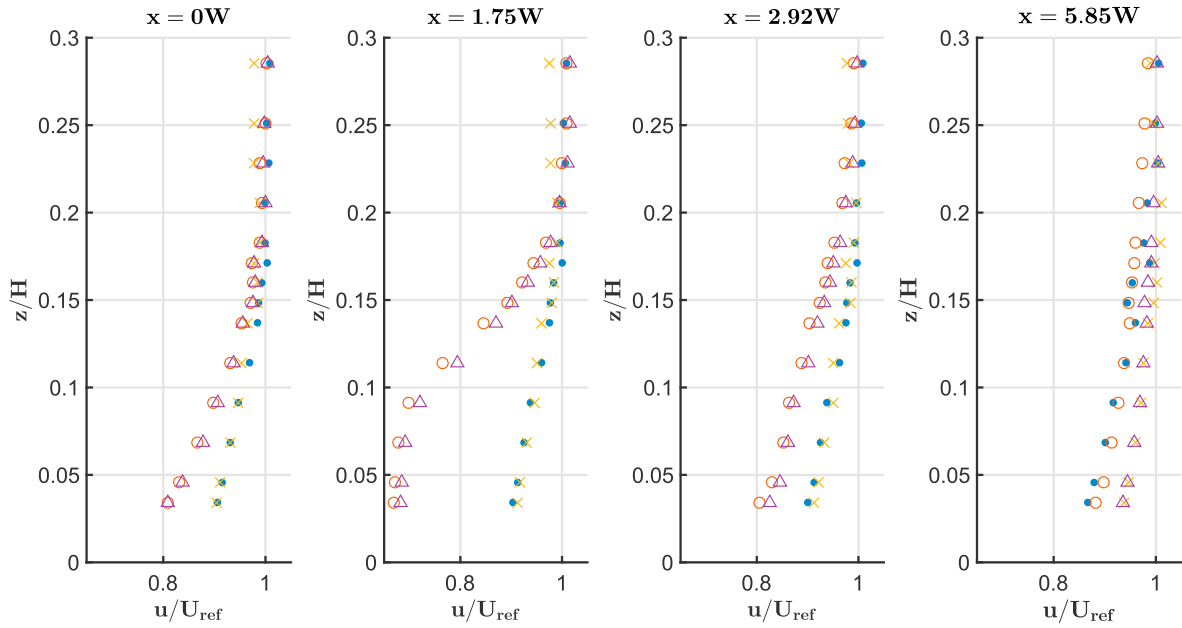


Fig. 23. Top surface's Boundary layer  $u$  velocity profile. ● - ( $G_f = 0.3W, G_r = 3.23W$ ). ○ - ( $G_f = 9.38W, G_r = 3.23W$ ). × - ( $G_f = 0.3W, G_r = 9.38W$ ). △ - ( $G_f = 9.38W, G_r = 9.38W$ ).

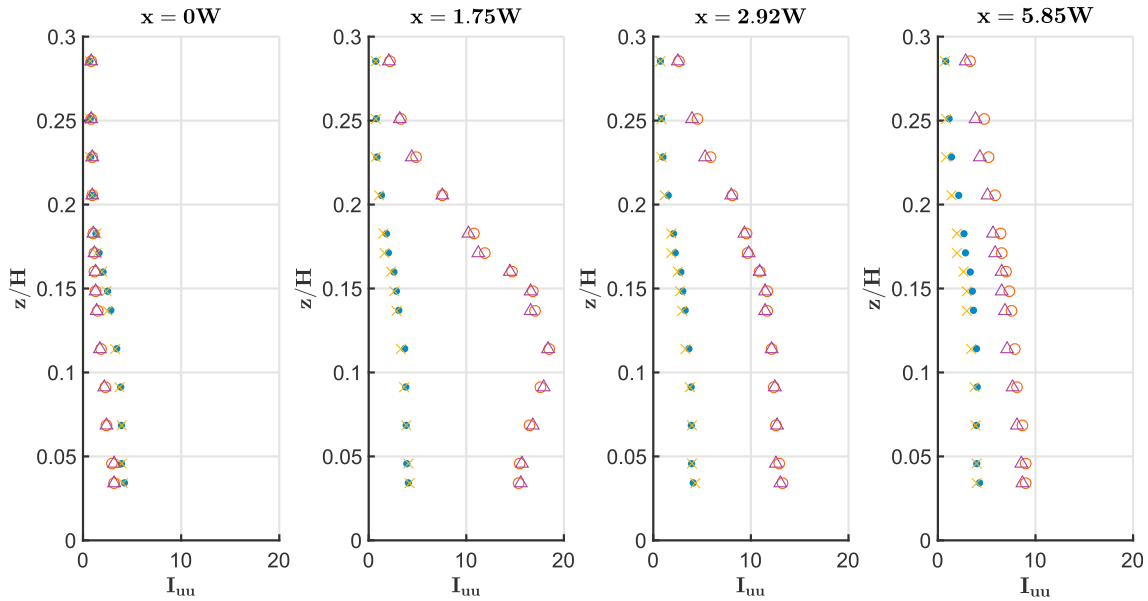


Fig. 24. Top surface's Boundary layer  $u$  component turbulence intensity. ● - ( $G_f = 0.3W, G_r = 3.23W$ ). ○ - ( $G_f = 9.38W, G_r = 3.23W$ ). × - ( $G_f = 0.3W, G_r = 9.38W$ ). △ - ( $G_f = 9.38W, G_r = 9.38W$ ).

$$C_p = \frac{P - P_{static}}{P_{dynamic}} \quad (3)$$

The uncertainties in the fluctuating pressure measurements are affected by both the static pressure uncertainty and those that arise from the use of a transfer function. As the transfer function is determined based on the tubing length and internal diameter the uncertainty is also a function of these properties, the latter being difficult to characterize for PVC tubes. The manufacturer provides an estimate of ( $\pm 2\%$ ) accuracy for frequency amplitude, depending upon tubing dimensions. However, in experiments by Irwin et al. (1979) it was found that the application of an inverse transfer function method, as used here, to pressure measurements through PVC tubes of internal diameter 1.35 mm resulted in an average error of 4.1% of the predicted peak pressure for a tubing length of 3 m, and 1.6% for tubing of length 0.61 m.

The accuracy of the cobra probe is stated to be  $\pm 0.5$  m/s. As all velocity results are normalised by the free-stream velocity the uncertainties of the presented results are:

$$\Delta \frac{u}{U_\infty} = \Delta u \times \frac{1}{U_\infty} \quad (4)$$

A summary of the estimated measurement uncertainty values for the key parameters investigated following the propagation methods described in ((Holman and Gajda, 1994)) are given in Table 8.

### 3.8. Limitations and future studies

The primary limitations of this study arise from difficulties in reproducing, in a wind tunnel, the flow conditions, that might be experienced

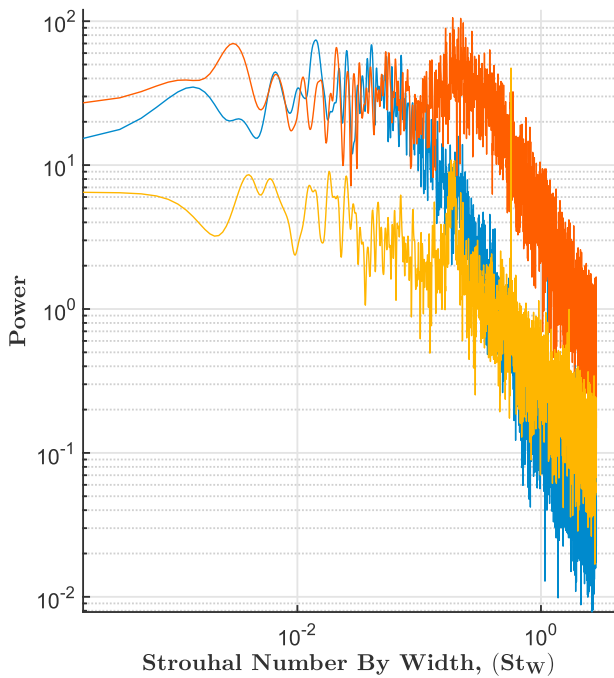


Fig. 25. Frequency spectrum of pressure taps located on side surface. — At leading edge ( $x = 0W$ ). — R2 Reattachment position ( $x = 2.46W$ ). — At trailing edge ( $x = 5.85W$ ).

by a train in the field. These include the moving ground reference, cross-wind component (yaw), freestream turbulence, Reynolds number, train length, range of wagon configurations, and geometric details of wagon (e.g. bogies) and the track itself (including ballast). In part these relate to the necessary reduction of parameter space considered herein, and in part are simplifications related to the wind tunnel testing. From a flow measurement perspective we were unable to characterise the reverse flow that exists in separated regions including the recirculating flow

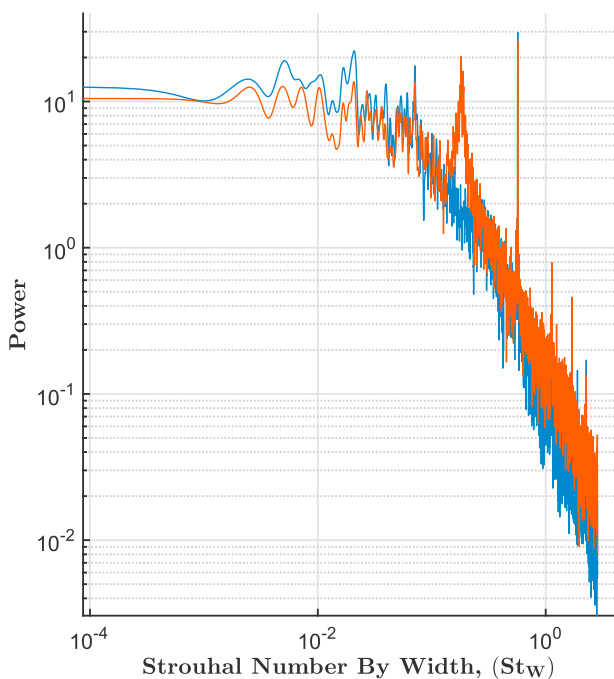


Fig. 26. Frequency spectrum of pressure taps located at the right edge ( $Z/H = 0, y/W = 0$ ) and at the mid point ( $Z/H = 0, y/W = 0.5$ ) for an isolated wagon in free-stream. — ( $Z/H = 0, y/W = 0$ ). — ( $Z/H = 0, y/W = 0.5$ ).

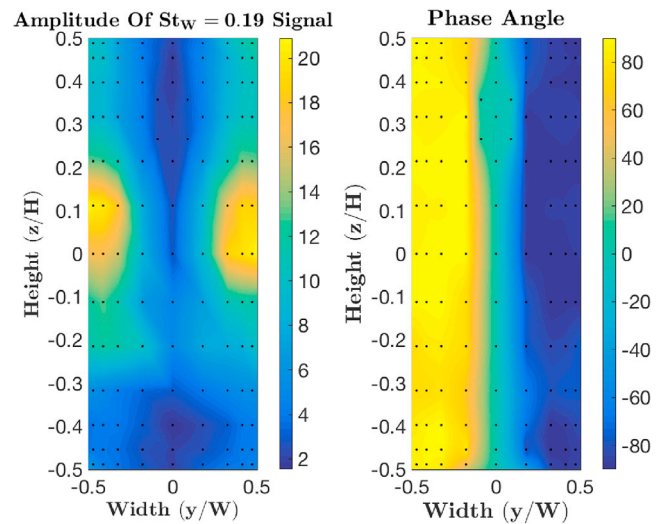


Fig. 27. The amplitude of the  $St_w \sim 0.19$  frequency is presented, along with the phase angle, both for an isolated wagon in free-stream.

within the gaps  $G_f$  and  $G_r$  because of the limited acceptance cone of the probe ( $\pm 45$  deg) and the invasive nature of these measurements. Following on from this work there remains a significant need to improve our understanding of the freight train aerodynamics, however such work will continue to require the application of a combination of tools: field data (such as freight train surface boundary profiles and wagon pressure distributions), correlated numerical studies and further wind tunnel investigations.

#### 4. Conclusion

The flow topology enveloping an isolated wagon in free-stream have features in common with that of a surface-mounted cube experiencing flow reattachment. The inferred flow structure of the leading-edge separation zones consists of three recirculation bubbles in the time-averaged sense, much like the those discovered by Martinuzzi et al. (Martinuzzi and Tropea, 1993). Similar to the cube, the front surface pressure consists of high stagnation pressure. The rear surface was covered by three bands of negative pressure zones, suggesting two spanwise vortices stacked vertically, with the bottom one impinging closer to the surface, as shown through LES simulations by Osth et al. (Osth and Krajnović, 2014).

It was shown, as expected, that as both gaps ( $G_f, G_r$ ) increased so does the drag of a double-stacked wagon, with the effect of front gap size the most significant. Drag coefficient changes were predominately associated with the local pressure acting on the surfaces adjacent to the gap. Increasing  $G_f$  increases the size of the leading-edge recirculation, increasing reattachment length for both R1 and R2. Turbulence levels in the boundary layer along the roof and sides of the wagon were augmented by large front gaps, this caused the subsequent wake of the wagon to be contracted, pushing the low-pressure core closer to the rear

Table 5  
Non-dimensional shedding frequency ( $St_w$ ) detected by the pressure tap on the front surface.

		$G_f$			
		3.23W	6.46W	9.38W	12.61W
$G_r$	0.30W	0.19	0.25	0.26	0.27
	1.04W	0.19	0.24	0.25	0.27
	1.77W	0.19	0.25	0.25	0.27
	3.23W	0.19	0.25	0.25	0.27
	6.46W	0.20	0.25	0.26	0.27
	9.38W	0.19	0.25	0.25	0.27
	12.61W	0.19	0.25	0.26	0.27

**Table 6**  
Shedding frequency ( $St_w$ ) detected on the rear surface.

		$G_f$						
		0.30W	1.04W	1.77W	3.23W	6.46W	9.38W	12.61W
$G_r$	3.23W	0.19	0.18	0.18	0.17	0.15	0.16	0.16
	6.46W	0.22	0.21	0.21	0.20	0.18	0.19	0.19
	9.38W	0.22	0.22	0.21	0.20	0.18	0.19	0.19
	12.61W	0.22	0.22	0.22	0.20	0.18	0.19	0.19

**Table 7**  
Second shedding ( $St_w$ ) signal detected on the rear surface.

		$G_f$			
		3.23W	6.46W	9.38W	12.61W
$G_r$	0.30W	0.19	0.25	0.26	0.27
	1.04W			0.25	0.27
	1.77W	0.19	0.25	0.24	0.26
	3.23W		0.25	0.25	0.27
	6.46W		0.25	0.26	0.27
	9.38W		0.25	0.25	0.27
	12.61W		0.24	0.25	0.26

surface. As a consequence, larger  $G_f$  not only directly increased the front surface pressure, it also acted to slightly reduce the rear pressure. In contrast, larger  $G_r$  was found to have little impact on the flow topology, although it does lower the top/side surface pressure towards the trailing edge of the wagon, resulting in a thinner boundary layer at separation, and subsequently a lower rear pressure was induced. Therefore,  $G_r$  was

shown to only directly affect the rear pressure, having no noticeable impact on the front surface.

It was found that the position of the reattachment line R1 coincided with the position of the first local minima on the pressure standard-deviation profile. R2, on the other hand, coincided with the turning point towards the top of the pressure recovery.

Karman-like shedding occurred in the wake for rear gaps larger than 3.23W, and the wake shedding frequency was a function of both  $G_f$  and  $G_r$ . Increasing  $G_r$  increased the wake shedding frequency while increasing  $G_f$  decreased the same frequency. The shedding frequency originating from an upstream dummy wagon was picked up on the front face of the test wagon. This frequency increased as  $G_f$  was increased. We speculated that this increase in shedding frequency was due to a larger gap inducing a thinner boundary layer at the wagon's trailing edge, thereby lowering the effective width of the wagon and increasing the shedding frequency. The lowering of wake shedding frequency, due to larger  $G_f$ , may be due to changes in the side-surface boundary layer creating a wider effective width of the wagon, however this was not measured in this study and will require further investigation.

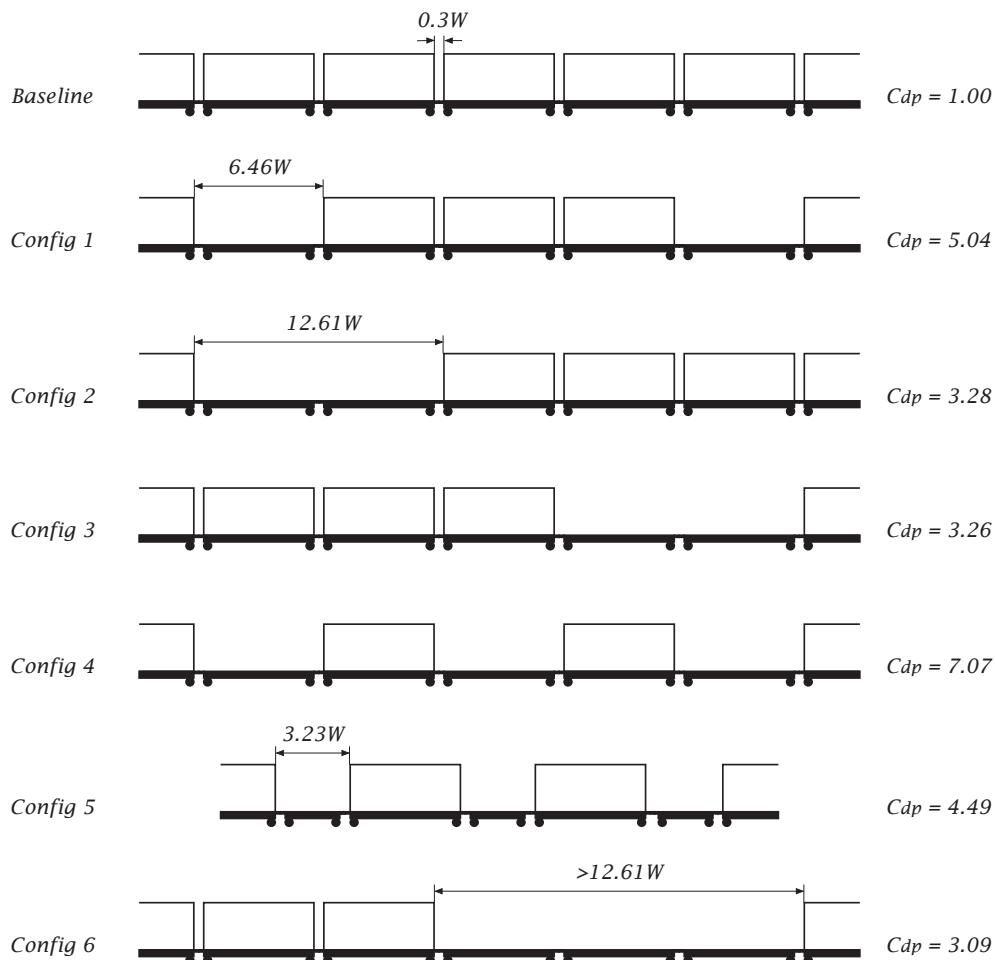


**Fig. 28.** Drag for different loading configurations.

**Table 8**  
Summary of estimated uncertainties for key parameters.

Descriptions	Parameters	Uncertainty ( $\xi$ )
Pressure (DPMS)	$p$	$\pm 0.4/1.6$ Pa
Local Pressure Coefficients	$C_p$	$\pm 0.004$
Front/Rear Pressure Coefficients	$C_{p_f}$	$\pm 0.009$
Pressure Drag Coefficients	$C_{Dp}$	$\pm 0.01$
Normalised Flow Velocity	$u/U_\infty$ (m/s)	$\pm 0.02$

Notably, the measured drag at the maximum gap sizes of  $G_f = G_r = 12.61W$  ( $C_{Dp} \approx 0.77$ ) did not fully return to that of a single isolated double-stacked wagon ( $C_{Dp} \approx 0.94$ ). Whilst further increases in  $G_f$  and  $G_r$  may cause some convergence, a wagon with upstream and downstream gaps has flat cars extending upstream and downstream, so that this case is different from an isolated wagon.

In terms of the aerodynamic efficiency of different loading configurations of trains, it was first demonstrated that reducing the number of gaps on a train is most beneficial. However, where gaps are unavoidable, as is often the case, this work indicates that it is more efficient to have a single large gap than to have multiple moderately sized gaps. This is because the drag penalty for a wagon, as a function of gap size, begins to plateau for gap sizes greater than  $6.46W$ . Front-surface pressure contours indicate a regime change in pressure distribution between  $G_f = 1.77W$  and  $G_f = 3.23W$ , this corresponded to the range with the greatest rate of drag increase. Therefore, for optimal drag reduction, it is recommended to reduce gap size to under  $1.77W$ . Further research is needed to account for wagons of different overall lengths, the specific position of the wagon within the train (subject to a different boundary layer thickness), crosswinds, and the effects of wagon geometrical details.

### Acknowledgement

This research was supported through Pacific National Rail and the Australian Research Council's Linkage Project funding scheme, under project number LP13100953.

### References

- Ahmed, S., 1983. Influence on base slant on the wake structure and drag of road vehicles. *J. Fluids Eng. Trans. ASME* 105 (4), 429–434.
- Baker, C.J., Quinn, A., Sima, M., Hoefener, L., Licciardello, R., 2014. Full-scale measurement and analysis of train slipstreams and wakes. part 1: Ensemble averages. *Proc. Inst. Mech. Eng. Part F J. Rail Rapid Transit* 228 (5), 451–467.
- Bearman, P., Morel, T., 1983. Effect of free stream turbulence on the flow around bluff bodies. *Prog. Aerosp. Sci.* 20 (2), 97–123.
- Bergh, H., Tijdeman, H., Theoretical and Experimental Results for Dynamic Response of Pressure Measuring Systems, National Aero and Astronautical Research Institute, Amsterdam, 328 (Report NLR-TRF).
- Camussi, R., Felli, M., Pereira, F., Aloisio, G., Di Marco, A., 2008. Statistical properties of wall pressure fluctuations over a forward-facing step. *Phys. Fluids* 20 (7), 075113 (1994–present).
- Castro, I., 1981. Measurements in shear layers separating from surface-mounted bluff bodies. *J. Wind Eng. Ind. Aerodyn.* 7 (3), 253–272.
- Castro, I., Robins, A., 1977. The flow around a surface-mounted cube in uniform and turbulent streams. *J. Fluid Mech.* 79 (02), 307–335.
- Cherry, N., Hillier, R., Latour, M., 1984. Unsteady measurements in a separated and reattaching flow. *J. Fluid Mech.* 144 (1), 13.

- Engdahl, R., Gielow, R., Paul, J., 1987. Train resistance-aerodynamics. In: *Intermodal Car Application. Railroad Energy Technology Conference II, vol. I of II, 1986*.
- Engdahl, R., Gielow, R., Paul, J., 1987. Train resistance-aerodynamics. In: *Open Top Car Application. Railroad Energy Technology Conference II, vol. II of II, 1986*.
- Gielow, M., Furlong, C., 1988. Results of Wind Tunnel and Full-scale Tests Conducted from 1983 to 1987 in Support of the Association of American Railroads' train Energy Program. Tech. rep.
- Golovanevskiy, V.A., Chmovzh, V.V., Girka, Y.V., 2012. On the optimal model configuration for aerodynamic modeling of open cargo railway train. *J. Wind Eng. Ind. Aerodyn.* 107, 131–139.
- Hammit, A., 1976. Aerodynamic Forces on Freight Trains. In: *Wind Tunnel Tests of Containers and Trailers on Flatcars, vol. 1. Tech. rep.*
- Hangan, H., Vickery, B., 1999. Buffeting of 2d (sharp-edged) bluff bodies. *J. Wind Eng. Ind. Aerodyn.* 82, 173–187.
- Havel, B., Hangan, H., Martinuzzi, R., 2001. Buffeting for 2d and 3d sharp-edged bluff bodies. *J. Wind Eng. Ind. Aerodyn.* 89 (14), 1369–1381.
- Hoarau, C., Boré, J., Laumonier, J., Gervais, Y., 2006. Analysis of the wall pressure trace downstream of a separated region using extended proper orthogonal decomposition. *Phys. Fluids* 18 (5), 055107 (1994–present).
- Holman, J.P., Gajda, W.J., 1994. *Experimental Methods for Engineers, vol. 2.* McGraw-Hill New York.
- Hudy, L.M., Naguib, A.M., Humphreys Jr., W.M., 2003. Wall-pressure-array measurements beneath a separating/reattaching flow region. *Phys. Fluids* 15 (3), 706–717 (1994–present).
- Irwin, H., Cooper, K., Girard, R., 1979. Correction of distortion effects caused by tubing system in measurements of fluctuating pressures. *J. Ind. Aerodyn.* 5, 93–107.
- Lai, Y.-C., Barkan, C., 2005. Options for improving the energy efficiency of intermodal freight trains. *Transp. Res. Rec. J. Transp. Res. Board* 47–55 (1916).
- Lai, Y.-C., Barkan, C.P., Onal, H., 2008. Optimizing the aerodynamic efficiency of intermodal freight trains. *Transp. Res. Part E Logist. Transp. Rev.* 44 (5), 820–834.
- Lai, Y.-C., Ouyang, Y., Barkan, C.P., 2008. A rolling horizon model to optimize aerodynamic efficiency of intermodal freight trains with uncertainty. *Transp. Sci.* 42 (4), 466–477.
- Leclercq, D.J., Jacob, M.C., Louisot, A., Talotte, C., 2001. Forward-backward Facing Step Pair: Aerodynamic Flow, Wall Pressure and Acoustic Characterisation. *AIAA paper* 2249, 2001.
- Li, C., Kost, M., Burton, D., Sheridan, J., Thompson, M.C., 2015. Wind tunnel investigation of a double stacked wagon in free-stream. In: *ASME/JSME/KSME 2015 Joint Fluids Engineering Conference, American Society of Mechanical Engineers. V001T16A002–V001T16A002*.
- Martinuzzi, R.J., Havel, B., 2000. Turbulent flow around two interfering surface-mounted cubic obstacles in tandem arrangement. *J. Fluids Eng.* 122 (1), 24–31.
- Martinuzzi, R.J., Havel, B., 2004. Vortex shedding from two surface-mounted cubes in tandem. *Int. J. Heat Fluid Flow* 25 (3), 364–372.
- Martinuzzi, R., Tropea, C., 1993. The flow around surface-mounted, prismatic obstacles placed in a fully developed channel flow (data bank contribution). *J. Fluids Eng.* 115 (1), 85–92.
- Maull, D., Young, R., 1973. Vortex shedding from bluff bodies in a shear flow. *J. Fluid Mech.* 60 (02), 401–409.
- Östth, J., Krajnović, S., 2014. A study of the aerodynamics of a generic container freight wagon using large-eddy simulation. *J. Fluids Struct.* 44, 31–51.
- Peters, J.-L., 1993. Effect of Reynolds number on the aerodynamic forces on a container model. *J. Wind Eng. Ind. Aerodyn.* 49 (1), 431–438.
- Ricciardelli, F., 1994. Aerodynamics of a Pair of Square Cylinders. *ME Sc. Thesis. Faculty of Engineering Science, The University of Western Ontario London, Ont., Canada*.
- Rowe, A., Fry, A.A., Motallebi, F., 2001. Influence of boundary-layer thickness on base pressure and vortex shedding frequency. *AIAA J.* 39 (4), 754–756.
- Sakamoto, H., Haniu, H., 1988. Aerodynamic forces acting on two square prisms placed vertically in a turbulent boundary layer. *J. Wind Eng. Ind. Aerodyn.* 31 (1), 41–66.
- Soper, D., Baker, C., Sterling, M., 2014. Experimental investigation of the slipstream development around a container freight train using a moving model facility. *J. Wind Eng. Ind. Aerodyn.* 135, 105–117.
- Sterling, M., Baker, C., Jordan, S., Johnson, T., 2008. A study of the slipstreams of high-speed passenger trains and freight trains. *Proc. Inst. Mech. Eng. Part F J. Rail Rapid Transit* 222 (2), 177–193.
- Watkins, S., Saunders, J., Aerodynamic Resistance and Design Principles for Unit Train Rail Vehicles, Railways of Australia Committee.
- Watkins, S., Saunders, J., Kumar, H., 1992. Aerodynamic drag reduction of goods trains. *J. Wind Eng. Ind. Aerodyn.* 40 (2), 147–178.